DESIGN AND PERFORMANCE ANALYSIS OF DIFFERENT PHOTONIC CRYSTAL FIBERS

By

Muntaha Rahman (170021065)

Mariea Sharaf Anzum (170021083)

Sadia Siraz (170021097)

A Thesis Submitted to the Academic Faculty in Partial Fulfillment of the Requirements for the Degree of

BACHELOR OF SCIENCE IN ELECTRICAL AND ELECTRONIC ENGINEERING

Department of Electrical and Electronic Engineering,

Islamic University of Technology (IUT),

Gazipur, Bangladesh.

May 2022

Declaration of Authorship

We, Muntaha Rahman (170021065), Mariea Sharaf Anzum (170021083) and Sadia Siraz (170021097), declare that this thesis titled, **DESIGN AND PERFORMANCE ANALYSIS OF DIFFERENT PHOTONIC CRYSTAL FIBERS,** and the works presented in it are our own.
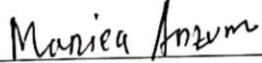
We confirm that:

- This work has been done for the partial fulfillment of the Bachelor of Science in Electrical and Electronic Engineering degree at this university.

- Any part of this thesis has not been submitted anywhere else for obtaining any degree.

- Where we have consulted the published work of others, we have always clearly attributed the sources.

Submitted By:

_____

Muntaha Rahman (170021065)

_____

Mariea Sharaf Anzum (170021083)

_____

Sadia Siraz (170021097)

DESIGN AND PERFORMANCE ANALYSIS OF DIFFERENT PHOTONIC CRYSTAL FIBERS

Approved by: ------------- *signature* 10-5-22 -------------------------------

Prof. Dr. Mohammad Rakibul Islam

Supervisor and Head

Department of Electrical and Electronic Engineering

Islamic University of Technology (IUT)

Boardbazar, Gazipur-1704.

Date: ……………………

ACKNOWLEDGEMENT

By the grace of our almighty Allah (SWT), we were able to complete our thesis with outstanding outcomes. We would like to express our gratitude and thank our thesis supervisor Md. Rakibul Islam, Professor Department of Electrical and Electronic Engineering, Islamic University of Technology for his constant support and guidance. We couldn't have asked for a better mentor to guide us on this journey. His helpful demeanor and patience are what helped us to carry on with our thesis work.

We are also thankful to all the faculty members of the Electrical and Electronic Engineering Department for their valuable advice, suggestions, and constructive criticism during the research wor.

Lastly, we can proudly say that today, we are in this position due to the several sacrifices made by our lovely parents. Their constant support and motivation are the backbone of our success and we are utterly grateful for that.

ABSTRACT

Over the years, countless designs of traditional PCFs and SPR-PCFs have been proposed by researchers with various structures, sensitivities, and confinement losses. However, a majority of such propositions depicted either large sensitivities but high confinement losses or low sensitivity and low losses. After an in-depth analysis of several previous works, keeping in mind their imperfections, we constructed our sensors and polarization filters with outstanding performance characteristics using Comsol Multiphysics 5.3a. We started our research by designing a typical hexagonal Photonic Crystal Fiber Sensor for milk detection showing a maximum sensitivity of 81.16% and 81.32% for camel and cow milk. We then went on to develop two different SPR-PCF sensors; a quadrature cluster SPR-PCF sensor attaining an outstanding ultra-high figure of merit (FOM) of 4230.42 RIU^{-1} and a Bent Core PCF-SPR sensor for broadband double peak sensing gaining maximum amplitude resolution of 1.18×10^{-6} RIU and a supreme wavelength resolution of 2.16×10^{-6} RIU. After working with sensors for an immense amount of time, we shifted our focus to other application aspects of PCFs, more specifically, polarization filters. We lastly suggested a D-structured single-polarization filter for S and U band applications. All of our designs have been optimized to achieve remarkable sensing and filtering characteristics like high sensitivity, meager losses, impressive FOM, satisfactory crosstalk and insertion losses.

TABLE OF CONTENTS

List of Tables

List of Figures

List Of Abbreviations

PCF : Photonic Crystal Fiber

SPR : Surface Plasmon Resonance

SPW: Surface Plasmon Wave

SP   : Surface Plasmon

SPP : Surface Plasmon Polariton

RIU : Refractive Index Unit

RI   : Refractive Index

NIR : Near-infrared Region

TIR : Total Internal Reflection

TE   : Transverse Electric

TM   : Transverse Magnetic

FEM : Finite Element Method

PML : Perfectly Matched Layer

THz : Terahertz

AS   : Amplitude Sensitivity

WS   : Wavelength Sensitivity

LSPR: Localized Surface Plasmon Resonance

EML : Effective Material Loss

CL   : Confinement Loss

CLR : Confinement Loss Ratio

ER   : Extinction Ratio

NA   : Numerical Aperture

FOM : Figure of Merit

EMF : Electromagetic Field

CT   : Crosstalk

Chapter 1

Introduction

1.1 Background study

Optical biosensors have been extensively used over the past decade, due to their fast rate of detection, sensitivity, and sturdiness. During the 1980s, the first optical biosensor had been commercialized. The main concept behind the functioning of any optical sensor is that the light intensity varies due to the presence of samples which may be chemical, biochemical, etc. The biosensors can be classified into six distinct groups based on the signal transduction process: optical, magnetic, mass, electrochemical, micromechanical, and thermal sensors.

The optical biosensors have several benefits in contrary to traditional analytical techniques in providing an instantaneous and label-free diagnosis of analytes in a sensitive, definite, and economical manner. Optical biosensors are widely employed in medical care, clinical diagnosis, environmental inspection, and the biotechnology sector. The biosensing may be achieved in a label-free or label-based fashion. Label-free detection necessitates interaction of the unknown substance with the transducer for signal sensing while in the latter protocol, analytes are labeled and the signal is generated by colorimetric, fluorescent, or luminescent methods. Biosensors based on Surface Plasmon Resonance (SPR) are one of the latest label-free optical sensing technologies [1].

Surface plasmons are surface charges that are created as an evanescent field travels along the juncture between a plasmonic metal and dielectric after an electric vibration took place. The evanescent field passes incident on the plasmonic metal surface excites its free electrons. A resonance condition occurs at a specific resonant wavelength when a balance between the frequencies of free electrons and a light photon is established. At this point, a sharp loss peak will be observed [2]. Any variation in the refractive index (RI) of the analyte will result in a corresponding change in the resonant wavelength.

Over time, SPR-based biosensors have contributed to various practical applications starting from the analysis of medicine, food quality, identification of the unknown viruses, gaseous substances, organic chemicals, bio-molecular analytes environmental examination, and many more [3]. Most recently, the resonance principle of such sensors has been utilized to design polarizing filters. These are optical equipment that split light by its polarization properties, and are mainly used in optical setups that need the effective regulation of the core

modes [4]. Filters displaying high extinction ratio, broad bandwidth, high crosstalk, and minimum insertion loss are being proposed.

1.2 Problem Statement

Over the past years, several designs of SPR based sensors have been proposed by several researchers. PCF-SPR sensors can be categorized into two groups depending on the plasmonic material used, i.e internal and external metal coating. In the case of internal coating, the fabrication is very difficult and liquid insertion in the air holes can limit their practical implementation. To avoid such problems, D-shaped externally coated sensors were proposed. However, the flat side requires polishing which increased the fabrication expenses. Thus, externally coated circular PCF-SPR sensors have gained the attention of everyone in recent times. Nevertheless, achieving high sensitivity with minimal loss is still a challenge for such sensors. Hence, there are several limitations of these sensors such as:

- Large loss
- Fabrication difficulty
- High sensitivity
- Complex structure
- Practical implementation expensive

1.3 Research Objective

 Investigation of SPR based PCF sensors is the most modern approach to sensing nowadays since the study of conventional photonic crystal fibres (PCF) have become quite outdated and the field is saturated. Hence, the key objective of our research was to explore various designs of SPR sensors and how their several characteristics were affected by their geometric parameters. Then, we went on to simulate our own sensor with the best performance parameters. The next step was to further investigate the application prospects of SPR-PCFs. Polarization filters based on SPR-PCF are the most popular optical applications of the fibers so we analyzed in-depth the design and functioning of such filters.

The main goals of our research have been summarized as follows:

- Conducting investing on various previous works on SPR sensors and polarization filters
- Use of plasmonic materials external to the PCF structure for better detection & performance.
- Using different combinations of plasmonic materials
- Proposing our design with the best outcome
- To examine the performance of our designs based on the wavelength/amplitude interrogation method and crosstalk the filter

- Comparison between our work with other previous designs proposed.

1.4 Motivation

SPR based PCF sensors and biosensors have become a hot research field due to its flexible geometry, single-mode transmission, broad tuning range, great temperature stability, low loss, and high birefringence. These sensors can be exploited in a wide plethora of application sectors such as healthcare, food, and environmental safety, gas detection, analyte detection, etc [5]. The geometrical parameters and plasmonic material adopted in these sensors can also be varied to achieve high performance, i.e. high sensitivity. As we can see, there is a huge scope for further investigation of these sensors. Furthermore, the recent use of PCF as polarization filters has gained recognition in the optic telecommunication industry.

1.5 Thesis Framework

A brief overview of all the chapters in this book has been given below.

CHAPTER-2 provides an in-depth analysis of photonic crystal fibers and the reason behind their extensive use. It discusses their several guiding techniques and also explains the different structures of PCF based on their core shapes.

CHAPTER-3 delivers an idea on the more advanced SPR technology and why this technology is more preferable to traditional PCFs. It also gives a clear explanation of the working principle of SPR and how SPR-based PCFs can be used as sensors and biosensors in practical applications.

CHAPTER-4 introduces the concept SPR-PCFs being used as polarization filters, their working principles, and application aspects.

CHAPTER-5 provides the fundamental equations that are needed for the investigation of PCFs, SPR based PCF sensors, and polarization filters. Important equations like Sellmeier equation (for RI of silica), Drude–Lorentz model equation have been explained. Also for analyzing the sensors' performance, its' several important parameters have been explored such as confinement loss (CL), wavelength/amplitude sensitivity, resolution, birefringence, crosstalk, insertion loss, etc. Finally, a study of the several materials (gold, silica, air) used in these fibers has been done.

CHAPTER-6 portrays our first research work which was a wheel structures hexagonal core PCF sensor used for milk sensing in the dairy industry. Its several geometrical parameters of the sensor such as core diameter, strut size, porosity, etc have been tuned to achieve the best sensing performances of this sensor. Finally, our sensor has been compared with several previous works.

CHAPTER-7 displays another work of ours which is a quadrature cluster SPR-PCF sensor for multipurpose. Various fiber design parameters bimetallic layer thickness, air hole diameter, and pitch distance have been optimized to improve the sensitivity of the sensor. Finally, the plethora of uses of this sensor to sense RI of analyte, temperature and magnetic field strength have been explored.

CHAPTER-8 illustrates yet another of our designs of a bent-core LSPR-PCF sensor for wideband double peak sensing. The sensors' two different geometries have been fine-tuned to obtain the highest amplitude and wavelength resolution. Apart from that, its double peaks have been exploited to introduce a completely novel sensing parameter called double peak shift sensitivity.

CHAPTER-9 gives an overview of our latest work on a D-shaped single-polarization filter for S and U band applications. Here, certain filter characteristics such as its cross-talk (CT), insertion loss, and output power have been studied by optimizing its design dimensions. Finally, its unique application in the S and U bands of the electromagnetic spectrum has been highlighted.

CHAPTER-10 discusses the future scopes of our thesis work and draws a conclusion to all of our works.

Chapter 2

Photonic Crystal Fiber

2.1 Introduction

Optical fibers are the backbone of the present-day telecommunication system. In any communication. They are the primary media to transmit data over long distances at higher bandwidths than electrical cables. These fiber channels have a loss of 0.2 dB/km at 1550 nm. The bandwidth of a single optical fiber link is roughly 50 THz[6]. However, because of some drawbacks of conventional optical fibers such as low refractive index differences and large leakage loss, photonic crystal fibers (PCF) were introduced to tackle these issues. The idea of a PCF was first brought to attention back in 1978 by Yeh *et al*. He suggested enclosing a fiber core with Bragg grating, grating, which is close to one dimensional photonic crystal.

PCF is a kind is a special class of optical fiber, consisting of the fiber core enclosed by a cladding, and air holes [7]. They have an adjustable geometry and outstanding wave guiding properties. They have a periodic ordering of low refractive index material (core) surrounded by a cladding with higher RI. The background material used is generally pure silica and the low-index is due to air capillaries inserted along the entire length of the fiber [6]. Also, altering the shapes of air holes severely affect the guiding characteristics of the fiber. The geometry of the core and cladding areas also play an essential part in the operation of the fiber. A lot of even and uneven structures of PCF like square, elliptical, hexagonal, decagonal, octagonal, and kagome have been designed to achieve highly efficient guiding mechanism and to use these fibers in a variety of applications. The porous core fibers have been gained more attention due to their meager effective material loss (EML), high birefringence, and higher core power fraction. Thus, simply by tuning the geometry, several designs of PCFs are possible.

2.2. Photonic Crystal Fiber (PCF)

Photonic crystal fibers (PCFs) are a unique category of optical fibers which are distinguished by a periodical ordering of air holes that form the fiber's cladding encircling a solid or hollow core [6].

2.2.1 Brief overview

In the recent times, there have been extensive research on PCF sensors in medical imaging, telecommunication, healthcare, spectroscopy, chemical and bio sensing, environmental monitoring, and drug testing [8]. PCFs can be classified, based on the core design, into **Fig. 2.1 (a)** solid and **(b)** hollow core fibers. Under these two classes, several structures are possible. The lattice arrangement, pitch (air hole to hole distance), and air hole size can be varies to suit the design specifications and functional requirements. PCFs with a solid core have a low-index

cladding encircling a core with a higher effective index. On the other hand, the hollow core fibers have a core with a lower index in comparison to the cladding medium, and light restriction to the core is done by scattering and interference, merging to create an evanescent field in the cladding.
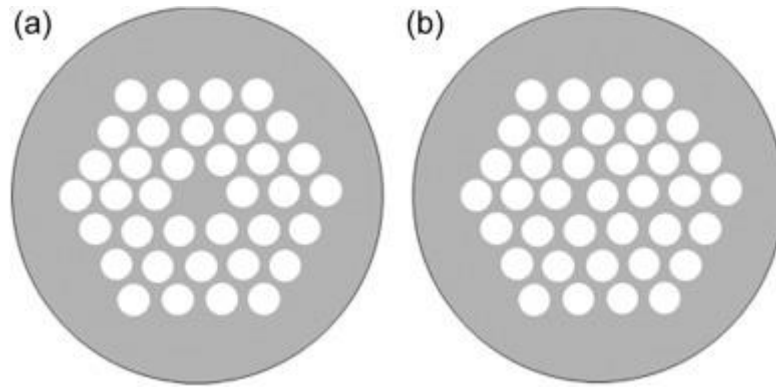
Fig.2. 1. Cross-sectional view of (a) solid and (b) hollow core PCF

2.2.2   Guiding mechanisms

In a conventional optical fiber, light transmits through the fiber by total internal reflection as the refractive index of the core is greater than that of cladding, thus light is restricted within the core. In photonic crystal fiber (PCF), however, two different light guiding mechanisms can be seen, depending on the structure.

In the case of solid core PCFs, a modified total internal reflection similar to that in conventional fibers is used, since light is constricted to the core. Here, the refractive index of the core material can be made larger than the cladding by making the core using silica solid. The core is encircled by a cladding filled with a network of air capillaries which lower its refractive index. These fibers, also called index guiding PCFs, direct the light using a process called modified TIR.

On the other hand, in hollow core fibers, photonic band gap mechanism is exploited. In this guiding mechanism, the core contains air holes which lower its refractive index than the cladding. Thus, light travels due to the existence of bandgap. We know that the photonic crystal permits only photons with a bandgap higher than that of cladding region. So, all those photons evanescent in cladding region and the others travel through the core.

2.3 Conclusion

PCF structures have recently gained popularity due its geometrical flexibility and wave guiding mechanisms. Ths chapter has briefly explained the mechanism of PCF. We have designed four structres so far on the basis of photonic crystal fiber which are explained in the upcoming chapters. The next chapter has explained the SPR phenomenon broadly.

Chapter 3

Surface Plasmon Resonance

3.1 Introduction

Surface plasmon resonance (SPR) is a phenomenon where the electrons at the surface of a metal layer are incited by the photons of incident light with a particular angle of incidence and then they travel along the metal surface.

3.2 Working principle of SPR

Surface plasmon resonance initiates when a photon of directed light incidents on a metal surface, called the plasmonic material. At a particular incident angle, a fraction of the light couples with the surface electrons, which are then excited to move. The motion of the electrons are now called plasmons, and they propagate along the metal surface. A portion of this light energy is reflected from the metal.

The angle of incidence is hypersensitive to slight variations in refractive index at the surface, as well as the depth of the analyte and gold layers. Hence, the analyte can be identified by evaluating the alterations in the reflected light falling on a detector.

3.3 Reasons behind interest in SPR technology

SPR sensors have a diverse range of functions ranging from biological/chemical identification, food safety, and environmental tracking. They can also be employed as optically adjustable filters, optical modulators, and sensors operating in the terahertz regime. They are mainly dominating over conventional PCFs due to their i) instant detection capacity ii) greater accuracy iii) real-time monitoring and iv) label-free detection

3.4 Literature review

This section explains surface plasmon wave (SPW) and evanescent field which are the key components to generate SPR effect.

3.4.1 Surface Plasmon Wave

When the frequency of the electrons at the metal surface matches that of the light photons, the electrons get excited. The vibration of these electrons is what generates an electromagnetic wave called a Surface Plasmon Wave (SPW) which transmits parallel to the surface.

The angle at which light is incident on the metal surface to maintain the SPW is highly dependent on the refractive index (RI) at the surface. Hence, small changes in RI can significantly alter the reflected wave which is the basic principle of SPR phenomenon.

3.4.2 **Evanescent field**

Optical sensors apply the idea of total internal reflection (TIR) to confine the light within the core and transmit it from one end to another. For light reflecting at angles close to the critical angle, a comparable amount of the power goes to the cladding medium. This phenomenon is called the evanescent wave. Its energy exponentially decreases as it moves through the cladding. This field has been utilized to allow real-time interrogation of surface-specific identification occurrences.

This idea of the wave extending further into the cladding area, allows the evanescent wave to interact more effectively with substances around the core far from its boundary.

3.5 Advantages of SPR technology

Some of the benefits for which the SPR technology received massive interest among researchers are as follows:

i. **Label-free detection** – SPRs do not require the use of labels to perform detection. Instead, they utilize the differences in refractive index to detect the analytes. One can inspect, in actual time, biomolecular interactions among proteins, RNA/DNA, and tiny molecules.

ii. **Recyclable sensor chips -** The chips directly affect the standard of the data and act as a very important part of biosensing. Since so much depends on the standard and performance of the sensor chip, it is amazing that these chips can be recycled.

iii. **Small sample sizes –** SPRs require only very small amounts of samples to perform their operation which is cost-effective, allows researchers to use less expensive materials.

iv. **Ability to manage complex samples** - Surface plasmon resonance can even be used in instances where only unrefined samples are available. SPR has been used for examining samples in a range of complex matrices including for serum analysis.

v. **Ability to replicate measurements** - Duplicate injections of similar concentrations of sample throughout a run can be done over and over again. Between day measuremnts of rate constants are also found to be similar, increasing confidence in the accuracy of results.

vi. **Real-time monitoring** – The SPR allows an inexpensive means to observe how various biomolecules interact in real-time. This has stupendous usages in the pharmaceutical and medical industries and also in areas like genetics and kinetics. Applications adopting nanoparticles are also gaining recognition.

3.6 Few disadvantages of the technology

The SPR biosensor technology has a few drawbacks also. Firstly, since biosensors depend on the existence of active biological molecules meaning the molecule must be active to produce a signal, unlike other analytical technologies such as mass spectrometry or UV spectrometry. Another demerit is that, although biosensor instruments are simpler to use, designing and executing an assay also needs some biochemistry skills.

3.7 Conclusion

A brief explanntion of SPR is provided in this section stating its advantages and recent advancement. Using this phenomenon, we have designed three prospective structures and these are explained in the later chapters. The upcoming chapter givesa short description regarding the polarization filters which are usually built on the basis of SPR in a photonic crystal fiber structure.

Chapter 4

PCF Polarization Filters

4.1 Overview of Polarization Filters

Currently, the design and investigation of photonic crystal fiber (PCF) is the hottest trend in optical fiber devices. PCFs do have unprecedented properties such as single-mode operation, adjustable birefringence, broad effective mode area, flexible nonlinearity, and tunable dispersion behavior. The application of SPR based PCFs is not only limited to sensing applications.

In SPR effect, the SPP mode couples with one of the core modes (i.e. x- and y- modes) at the resonance wavelength where a maximum loss peak is observed. This idea of coupling can be utilized in filtering applications, optical sensing, and sub-wavelength applications. This is achieved by creating a large birefringence in the fiber by creating an asymmetry arrangement of the air holes. This provides us with the option of designing polarization components [9].

In the filtering activity, either of the two polarization modes (x- or y-polarizations) is restricted from transmission due to its significantly higher loss in comparison to the other state[10]. Therefore, in modern optoelectronic and communication schemes, these filters play a major part in the field of passive optical networks. Such filters are intended to mainly operate at the optical communication wavelengths of 1310 nm and 1550 nm.

4.2 Conclusion

A brief explanation of polarization filters is provided in this section stating its advantages and recent advancement. Using this phenomenon, we have designed one prospective structure and it is explained in the later chapters. The upcoming chapter gives a short description regarding the mathematical formulas of the performance parameters and also the characteristics of the materials used.

Chapter 5

Mathematical interpretation

5.1 Introduction

Different parameters have been employed for the formulation of our entire project. Several behavioral parameters of the photonic crystal fiber-based structures can verify their performances. In this section, we have attempted to formalize different aspects, including sensitivity (%), core power fraction (%), effective area (A_{eff}), effective refractive index, effective material loss (EML), numerical aperture, dispersion, confinement loss (CL), which are the basic features of a PCF based sensor. In contrast, wavelength sensitivity (WS), magnetic field sensitivity, amplitude sensitivity (AS), resolution, temperature sensitivity, and the figure of merit (FOM), etc., can evaluate the sensor performance based on SPR. Additionally, to investigate our suggested design for PCF-SPR-based filters cross-talk (CT), Extinction ratio (ER), the output power can be taken into account apart from confinement loss. The equations that can be utilized to characterize the materials used for our project have been demonstrated in the later section of this chapter. It's worth noting that these materials' refractive index (RI) is our only point of focus. As a result, we've just presented the RI equations for these materials. We've included permittivity equations in some circumstances because the square root of permittivity equals the RI.

5.2 Computational study of Performance Parameters

5.2.1 Conventional PCF sensors' characteristics

5.2.1.1 Confinement loss (CL)

One of the most crucial performance statistics for measuring PCF sensor performance can be termed as confinement loss because it is required to evaluate all other metrics. The CL denotes the energy diverted from core mode to SPP mode by modified total internal reflection (MTIR). Confinement losses are caused by the imperfect structural design of the PCF. A part of the light energy dispatched through the PCF sensor's core reaches the metallic layer seeping from the core. The CL is the quantity of energy that is lost as a result of this leakage which can be qualified by [11]-

$$\alpha(dB/cm) = 8.686 \times \left(\frac{2\pi}{\lambda}\right) \times \text{Im}(n_{eff}) \times 10^4 \tag{5.1}$$

The $\text{Im}(n_{eff})$ is expressed as the effective mode index's imaginary part whereas, λ denotes the wavelength. The phase-matching condition occurs when the real component of the effective RI for

the core and SPP mode become identical at resonance wavelength. The surge appears to be the confinement loss spectra that can be used to formulate the basis of PCF-SPR sensors and polarization filters.

5.2.1.2 Effective Material Loss (EML)
The effective material loss (EML) is one of the most important key performance parameters for a PCF. A minimum level of material absorption loss is required to develop the sensing abilities of a sensor for the waveguiding in the THz region. The formula $\alpha(v) = v^2 + 0.63v - 0.13$ (dB/cm) can explain the linear relationship between EML and frequency (v) [12].

5.2.1.3 Relative Sensitivity
One of the most essential aspects in determining the PCF's adaptability is its relative sensitivity. It defines how much light contacts with the specimen of an analyte. The given formulation can be used to evaluate it quantitatively[13].

$$r = \frac{n_r}{n_{eff}} \times P\% \tag{5.2}$$

Where the RI of the analyte and effective RI is n_r and n_{eff}, respectively. P stands for the power fraction, which is the ratio of % of the power of the air hole to overall power. The given expression can be used to compute it [14]:

$$P = \frac{\int_{sample} R_e(E_x H_y - E_y H_x)dxdy}{\int_{total} R_e(E_x H_y - E_y H_x)dxdy} \times 100 \tag{5.3}$$

Where E_x, E_y are the transverse electric fields, and H_x, H_y are the transverse magnetic fields for the fundamental guided mode.

5.2.1.4 Effective cross-sectional area (A_{eff})
The effective area is the best estimate of the area within the core that is constricted by light. Within this zone, electromagnetic waves propagate. The mathematical methodology can be used to measure effective area accurately [14]:

$$A_{eff} = \frac{[\int I(r)r\, dr]^2}{[I^2(r)\, dr]^2} \tag{5.4}$$

The transverse electric field's intensity distribution can be termed as $I(r) = |E(t)|^2$.

5.2.1.5 Effective refractive index (n_{eff})
The effective refractive index is the ratio of the speed of light in air to the speed of light in the media for the particular polarization to the direction of the axis of propagating light via the guiding structure. Any material's effective RI can be calculated using the formula below. [15]-

$$n_{eff_{pm}} = \frac{c}{v_{zpm}} = \frac{\beta_{pm}}{k_0} \tag{5.5}$$

Here, the propagation constant is defined as β_{pm}, And the quantity of waves in a void is $k_0 = \frac{\omega}{c}$ $= \frac{2\pi v}{c} = \frac{2\pi}{\lambda_0}$ Whereas v is the frequency, and wavelength is expressed as λ_0.

5.2.1.6 Numerical Aperture

The numerical aperture of fiber is an assessment of its light interaction strength. For a PCF sensor, a greater numerical aperture is preferable since it enhances the light constriction inside the core. The numerical aperture is determined by the following relationship where c, f is the velocity of light and frequency whereas A_{eff} is the effective area [14]-

$$NA = \frac{1}{\sqrt{1 + \frac{\pi A_{eff} f^2}{c^2}}} \tag{5.6}$$

5.2.1.7 Dispersion

As light travels along the route of a fiber, dispersion describes how light pulses spread out. Dispersion can be divided into two types. Material and waveguide dispersion are the two factors at play. For our project, waveguide dispersion is taken into consideration, which is measured by [16] -

$$\beta_2 = \frac{2}{c} \frac{dn_{eff}}{d\omega} + \frac{\omega}{c} \frac{d^2 n_{eff}}{d\omega^2} \tag{5.7}$$

Where angular frequency is ω, and the rest of the parameters have been already mentioned in the earlier section.

5.2.2 SPR-PCF based sensors' characteristics

5.2.2.1 Amplitude Sensitivity

The wavelength and amplitude interrogation techniques are two ways of determining the sensor potential. The variation in loss depth caused by changes in the RI of the analyte can be used to identify unidentified specimens. The amplitude interrogation (intensity-based measuring) approach is a method for detecting different analytes.

$$s_A = -\frac{1}{\alpha(\lambda, n_a)} \frac{\partial_a(\lambda, n_a)}{\partial n_a} (RIU^{-1}) \tag{5.8}$$

Here, $\alpha(\lambda, n_a)$ is the confinement loss for a certain sample RI whereas $\partial_a(\lambda, n_a)$ signifies disparity in analyte confinement loss between two adjacent refractive indices [17].

5.2.2.2 Wavelength Sensitivity

The wavelength interrogator (spectral-based assessment) technique, which considers the fluctuation in resonance wavelength, is another way to assess the sensor's performance. When compared to the approach mentioned in the earlier section, this method usually has a higher sensitive response. The cost-effectiveness of the phase-detection method (WI method) is one of its

perks. However, there is a consequence, which is the difficulty of assessing sensitivity In this approach [18]. The underlying formula is used to calculate a sensor's sensitivity [19]

$$s_\lambda = \Delta\lambda_{Peak} / \Delta n_a (nm / RIU) \tag{5.9}$$

The discrepancy between adjacent resonant wavelengths and two refractive indices is expressed as in this scenario λ_{Peak} and Δn_a respectively.

5.2.2.3 Figure of Merit (FOM)

Aside from AS and WS, another measure referred to as the figure of merit is also utilized to estimate sensor efficiency. It's only the proportion between the WS (S_λ) and the FWHM [17]. The breadth of the confinement loss curve at half the peak loss is known as the FWHM. The sharpness of the loss peak is dictated by it. The sharper a sensor's loss peak, the superior its sensing efficiency.

$$FOM = \frac{S_\lambda}{FWHM} \left(RIU^{-1} \right) \tag{5.10}$$

5.2.2.4 Temperature Sensitivity
All of the preceding investigations are usually conducted at a constant temperature. However, in the real world, the weather, as well as the temperature, can change over time. To make the designs more interactive, we can use ethanol as a reagent to determine its temperature sensitivity. The equation can be used to predict temperature sensitivity [20]-

$$S_T = \frac{\Delta\lambda_{Peak}(T)}{\Delta T} (nm / °C) \tag{5.11}$$

Where $\Delta\lambda_{Peak}(T)$ is the temperature deviation of the RW peak while ΔT is the difference in temperature.

5.2.2.5 Magnetic Field (MF) Sensitivity
A magnetic fluid with a refractive index that is affected by the varied MF and temperature should be used to do this investigation. The RI variation of the fluid owing to altering MF and temperature can be calculated using the Langevin function [21]-

$$n = [n_s - n_b] \left[\coth\left(\alpha \frac{H - H_{c,n}}{T} \right) - \frac{T}{\alpha(H - H_{c,n})} \right] + n_b \tag{5.12}$$

T denotes temperature (Kelvin), H is magnetic field strength (Oe), $H_{c,n}$ represents critical field strength, α expresses fitting parameters, n_s defines saturated RI, and n_b can be termed as magnetic fluid's RI for magnetic field strengths less than $H_{c,n}$. The RI of the analyte changes to 1.3808 from 1.3337 as we employed an MF span with a 125 Oe intermission from 0 Oe to 1000 Oe.

The MF sensitivity can be attained from the formulation [22] -

$$S_H = \frac{\Delta\lambda_{Peak}}{\Delta H}\left(nm/Oe\right) \tag{5.13}$$

Where ΔH denotes the variance in the magnetic field.

5.2.2.6 Resolution

Resolution is a characteristic that aids in determining the sensor's recognition accuracy. The resolution indicates the magnitude of the smallest variation in RI that may be determined. It can be manifested w.r.t amplitude ($R(A)$), wavelength ($R(W)$), temperature (R_T) [2], [17], [20]-

$$R(A) = \frac{\Delta n_a}{s_A}\left(RIU\right) \tag{5.14}$$

$$R(w) = \frac{\Delta n_a}{\Delta\lambda_{Peak}} \times \Delta\lambda_{\min}\left(RIU\right) \tag{5.15}$$

$$R_T = \frac{\Delta T \times \Delta\lambda_{\min}}{\Delta\lambda_{Peak}}\left(°C\right) \tag{5.16}$$

Here all the terms are mentioned in the preceding sections except $\Delta\lambda_{\min}$ which defines the minimum wavelength resolution.

5.2.2.7 Novel dual peak shift sensitivity for structures having two consecutive resonance peaks

There can be sensor designs that may depict two distinct peaks for a particular refractive index (RI) of investigation due to the simultaneous usage of multiple plasmonic material layers (i,e. gold-AZO combination which will be discussed extensively in the forthcoming sections). A unique sensitivity factor named double peak shift sensitivity (s_{P-P}) is appointed, which is characterized by the subsequent formulations and extends the notion of two resonance wavelengths' (RW) peak to peak distance with analyte RI [23]-

$$S_{p-p} = \frac{\left(\lambda_{p2}-\lambda_{p1}\right)_{n_b} - \left(\lambda_{p2}-\lambda_{p1}\right)_{n_a}}{n_b - n_a} \times 10^3 \, (nm/RIU) \tag{5.17}$$

Or,

$$S_{p-p} = \frac{\left(\lambda_{p2,n_b}-\lambda_{p2,n_a}\right) - \left(\lambda_{p1,n_b}-\lambda_{p1,n_a}\right)}{n_b - n_a} \times 10^3 \, \left(nm/RIU\right) \tag{5.18}$$

Primary RWs for consecutive RIs n_b and n_a are λ_{p_1,n_b} and λ_{p_1,n_a}. Whereas, λ_{p_2,n_b} and λ_{p_2,n_a} represent the secondary ones.

5.2.3 SPR-PCF based polarization filters' characteristics

5.2.3.1 Cross-talk (CT)

One of the most important goals in filter design is to emphasize the discrepancy in confinement losses between the two polarized modes. This phenomenon is best explained by cross-talk (CT), hence a greater CT is recommended. It can also be used to evaluate the signal quality used by polarization filters, which is an essential parameter for calculating the effects of unwanted modes. The following equation can be used to describe it [24]-

$$CT = 20 \lg \left\{ \exp \left[(\alpha_2 - \alpha_1) L \right] \right\} \tag{5.19}$$

Where L expresses the fiber length and the corresponding CL of x-y polarization modes are α_1 and α_2.

5.2.3.2 Output Power (Pout)

When evaluating the filtering features of a polarization filter, one of the most crucial attributes to explore is output power. The following expression can be used to specify it where *Pin* is the input power, confinement loss is *Lc* [25]-

$$Pout(x, y) = Pin(x, y) \exp(-Lc(x, y) \times (\frac{\ln 10}{10}) \times L) \tag{5.20}$$

5.2.3.3 Extinction Ratio (ER)

The extinction ratio is crucial as it determines how well an optical fiber can maintain polarization. In decibels (dB), it compares the optical power on the desired axis to the optical power on the unwanted plane, the orthogonal polarizing condition. The ER is represented by the equation below [25] -

$$ER = 10 \log_{10} \left(\frac{Pout(y)}{Pout(x)} \right) \tag{5.21}$$

5.2.3.4 Confinement Loss Ratio (CLR)

The Confinement Loss Ratio (CLR) can be used to measure the filtering performance of a single polarization filter over a given spectral region. The following expression can be used to compute CLR -

$$CLR = \frac{Lc_x}{Lc_y} \tag{5.22}$$

5.3 Computational study of the materials used

5.3.1 Zeonex

Certain polymer materials, including topas, teflon, Zeonex, etc., are favored as bordering constituents in the PCF structures in terahertz applications to obtain improved effective area, high relative sensitivities, and increased core power fraction with lower confinement loss. However, in comparison to other materials, Zeonex should be employed as a background material because of its several significant features [26]-

- Fixed RI (1.529) for a broad span of wavelength
- Lesser absorption loss
- Improved transparency, absorption co-eff, dielectric loss tangents, and thermochemical stability.

5.3.2 Air

The PCF is filled with air to fill the voids. Air has a refractive index of almost 1 which remains real in all the cases, which means light travels through the environment at nearly the same speed as it does in a vacuum. We detect refraction with regard to the light path in the air because we are submerged in the atmospheric condition, and simple refraction experiments genuinely quantify Snell's Law with respect to air.

5.3.3 Fused Silica (SiO2)

Typically, SPR-based sensors are made by laminating plasmonic metal on the surface of a PCF. The PCF can be built out of either glasses or polymers. Fused Silica, also known as silicon dioxide, is the material of choice for the SPR-PCF background. In most cases, undoped silica is employed. Silica is preferred over other glasses and polymers because of its underlying beneficial characteristics [27]-

- Broader wavelength region possessing better optical transparency
- Lesser absorption and scattering losses
- Greater mechanical resilience
- Higher chemical stability
- Greater damage resistance

The RI of this surrounding component can be defined by the Sellmeier equation [20]-

$$n^2(\lambda) = 1 + \frac{B_1\lambda^2}{\lambda^2 - C_1} - \frac{B_2\lambda^2}{\lambda^2 - C_2} - \frac{B_3\lambda^2}{\lambda^2 - C_3} \qquad (5.23)$$

Here n represents RI which depends on the λ light wavelength. The corresponding values of the constants $B_1, B_2, B_3, C_1, C_2, C_3$ are 0.696, 0.408, 0.897, 0.0047 μm^2, 0.014 μm^2,and 97.934 μm^2 .

Moreover, the adjusted Sellmeier equation for a fixed temperature (T) of 25°C is defined as [20]-

$$n^2\left(\lambda, \text{T}\right) = \left(1.31552 + 6.90754 \times 10^{-6}\text{T}\right) + \frac{(0.788404 + 23.5835 \times 10^{-6}\text{T})\lambda^2}{\lambda^2 - (0.0110199 + 0.584758 \times 10^{-6}\text{T})}$$
$$+ \frac{0.91316 + 0.548368 \times 10^{-6}\text{T})\lambda^2}{\lambda^2 - 100}$$

(5.24)

5.3.4 Gold

Because of their high conductivity, metals are good options for plasmonic purposes. Silver and gold are the most frequently utilized metals for plasmonic usage due to their low value of loss in the near-infrared and visible scale. Moreover, silver or gold has been employed as the plasmonic substance in practically all of the key research investigations on plasmonics [28]. Other than these two materials have also been employed in plasmonics, but their application is restricted due to their larger losses. Silver, on the other hand, degrades swiftly when it comes to manufacturing. The other advantages that gold provides due to which we have given preference to it [28]–[30]-

- Chemical stability
- High stability in air
- Better sensitivity
- No oxidization unlike silver

The Drude-Lorentz model can define the gold's dielectric constant (ε_g)[31]-

$$\varepsilon_g = \varepsilon_\infty - \frac{\omega_D^2}{\omega(\omega + j\gamma_D)} - \frac{\Delta\varepsilon\Omega_L^2}{(\omega^2 - \Omega_L^2) - J\tau_L\omega}$$

(5.25)

Where, the angular frequency is ω, damping frequency, and permittivity are defined by $\gamma_D = 31.84\pi$ THz, $\varepsilon_\infty = 5.9673$, respectively. Whereas $\omega_D = 4227.24\pi$ Hz expresses the plasmonic frequency, and $\Delta\varepsilon$ provides weighting factor. Spectral width $\frac{\Gamma_L}{\pi}$ = 209.72 THz, and oscillator strength is denoted as $\frac{\Omega_L}{\pi}$ = 1300.14 THz.

5.3.5 AZO

Another plasmonic material used as a substitute for gold is aluminum doped Zinc Oxide (2% weight of Al in ZnO), also known as AZO. Despite the oxidation impact on aluminum in the hydrous area, it holds potential. AZO has several benefits over gold as a plasmonic material [29]-

- Higher doping results in decreased losses due to enhanced crystallinity in heavily doped layers
- For wavelengths higher than around 1.8µm, AZO exhibits metallic characteristics in the NIR
- The doping concentration can be changed to adjust the charge carrier density and hence the plasma frequency

The dielectric property of AZO can be expressed as-

$$\varepsilon_{AZO} = \varepsilon_b - \frac{\omega^2_p}{\omega(\omega + j\gamma_p)} + \frac{f_1\omega^2_1}{(\omega^2_1 - \omega^2 - j\omega\gamma_1)} \tag{5.26}$$

Where ε_b = 3.5402 is defined as the background permittivity and ω_p =1.7473 eV is the plasma frequency with f_1 = 0.5095, γ_1 = 0.1017 eV, γ_p =0.04486 eV, , ω_1 = 4.2942 eV.

However, dual plasmonic materials exhibiting gold and AZO can be specified to be used in conjunction to identify analytes with a diverse range of indices of refraction starting from the ultraviolet range to the infrared region. At resonance circumstances, gold and AZO can be combined at three different orientations to form separate double peaks (this phenomenon will be discussed thoroughly in the later sections)

5.3.6 Titanium dioxide (TiO2)

The use of a thin coating of titanium dioxide in between the plasmonic material and the fiber has gained popularity in recent years. The bimetallic layer will show some advantages [32]-

- Enhancement of surface plasmon response
- Accelerating the SPP and core mode coupling
- Alleviation of adhesion issue

The RI of TiO_2 can be defined as follows [19] -

$$n_t = \sqrt{5.913 + \frac{2.441 \times 10^7}{\lambda^2 - 0.803 \times 10^7}} \tag{5.27}$$

5.3.7 Ethanol

We're interested in ethanol because of its temperature sensitivity. Ethanol's refractive index is a real number that changes with temperature. Because of its temperature-sensitive characteristic, ethanol can be used to measure temperature. When the analyte of an SPR-based PCF sensor contains ethanol, the sensor can be used as a temperature sensor. As a result, we ought to determine ethanol's temperature-dependent RI, which may be written as [20]-

$$n_1 = n_0 + \frac{dn}{dT}(T_1 - T_0) \tag{5.28}$$

The ethanol's thermo-optical co-eff is $\frac{dn}{dT} = -3.117 \times 10^{-4} C^{-1}$. n_1 is the RI for temperature T_1 and for $T_0 = 20°C$, the RI is $n_0 = 1.361$. When we steadily lowered the temperature from 70°C to -70°C, the ethanol's RI varies from 1.3454 to 1.3891.

5.4 Conclusion

We are now acquainted with all of the materials needed to build an SPR-based PCF sensor. We've also learned how to evaluate sensor performance using the parameters we've learned. The characterization equations and performance characteristics for these materials are used in the next chapters to explain our suggested sensor construction and its performance.

Chapter 6

Proffered design 01: PCF sensor for dairy industry working in thz region with wheel structure

6.1 Introduction

In recent times, terahertz (THz) sensing has received a lot of interest. The THz region in the EM spectra changes to 10 THz from 100 GHz or from 3 mm to 30μm w.r.t wavelength. THz technology is rapidly progressing in telecommunication, spectroscopy, sensing, medical imaging, and other fields because of its non-destructiveness, low penetration depth, and non-invasiveness [33]. PCF sensors have a significant THz power coupling property with diverse analytes, resulting in increased sensitivity. It's an ideal option for THz sensing applications because of all of the unique properties like low scattering, lower loss, large core power fraction, etc. In this chapter, a novel PCF structure with a porous core for measuring cow and camel milk is proposed for the porosities of 98%, 90%, and 85%. The core's porosity is termed as the proportion of air vents in the core in comparison to the overall area of the core. The experiment is carried out in the spectral regime of 0.2 THz to 2.0 THz. The PCF structure is made up of a hexagonal-shaped core with air holes and a circular sectored covering. At f = 2 THz frequency, camel milk has maximal sensitivity of 81.16 percent and for cow milk, it is 81.32 percent, correspondingly. Milk from camels produces a confinement loss (CL) of 8.675×10^{-18} cm^{-1}, while that of cows gives a 1.435×10^{-18} cm^{-1} CL. Also, it achieved a flattened dispersion of 10.5 ps/THz/cm. Our developed sensor will be very desirable for sensing milk, based on fabrication feasibility and numerical results. No previous research has yielded PCF sensors for milk sensing, as we are aware. As a result, this form of the sensor can open up a whole new approach for the dairy sector. Furthermore, using THz power in milk sensing applications could provide new perspectives.

6.2 Design methodology and electromagnetic (EM) field distribution

The suggested Zeonex-based THz PCF sensor's 2D cross-sectional arrangement, as well as a thorough representation of the hexagonal core structure, are illustrated in Fig.6.1. The following fiber's design was done by the widely viable COMSOL Multiphysics 5.3b software, which is based on the finite element method (FEM). The symmetrical cladding framework consisting sixteen non-circular segments of air denoted by the letter s. The distance between each segment's end to endpoints is n. h stands for the height of each air segment. All parts have the same height, which is 2065 **μm**. In the core, there are nineteen circular holes organized hexagonally. Every circular hole's radius is designated by the letter r. In the central region, two hexagonal-shaped rings encircle the center's circular hole. The first ring has six air holes, whereas the second hexagonal ring has twelve circles as air holes. The separation between the two consecutive air holes in the same ring

is indicated by **Λ** and the separation between the two neighboring holes in the other ring can be represented as **Λ₁**. D$_{core}$ represents the diameter of the central region. The core part uses camel milk possessing a RI of 1.3423 and cow milk having a RI of 1.3459 as analytes. The suggested structure is encircled by a perfectly matched layer (PML) that allows waves to travel through avoiding reflection. It also serves as a coating that is anti-reflective. This PML is 5.7 percent of the fiber's overall radius.
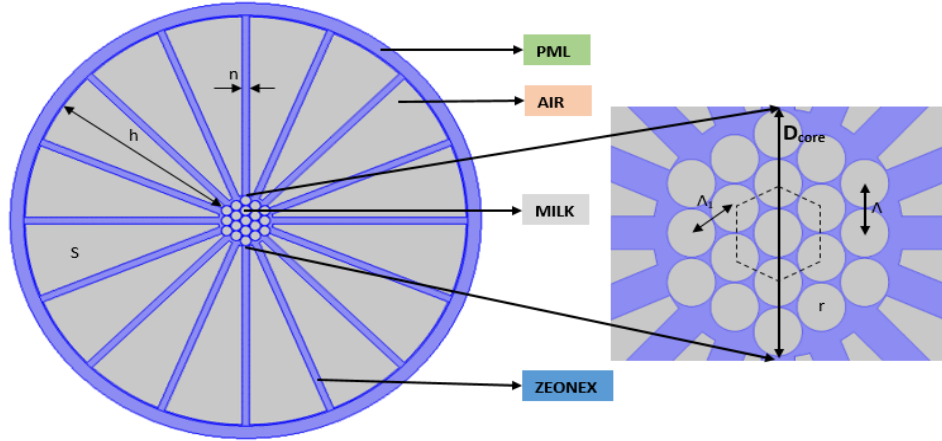
Fig 6.1: Cross-section of the proposed PCF structure for milk sensing
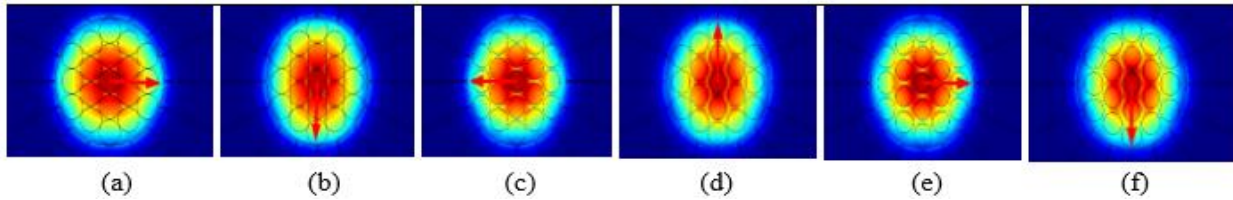
Fig 6.2: Light energy distribution for 98% porosity (a) x-pol (b) y-pol, for 90% porosity (c) x-pol (d) y-pol, for 85% porosity (e) x-pol (f) y-pol

The EM field distribution for the suggested device was recorded within a spectral regime of 0.2 THz to 2.0 THz, with camel milk and cow milk as the intended analyte, as seen in figure 6.2. The light appears to be restrained inside the core, showing a strong interplay between the core and analyte for both modes, but limited contact within the cladding portion.

6.3 Results and discussion

6.3.1 Sensitivity (%) analysis

Figure 6.3a shows the impact on the sensitivity of different frequencies of the PCF when using milk of cow for the analyte. The sensitivity increases with increasing up to 1.4 THz frequency, beyond which it becomes constant. This effect is produced by the attributes of higher-frequency EM signals, which always attempt to propagate on the inside of vicinity with a higher RI. More light propagates through the core and is consequently contained inside the core region as frequency increases, creating stronger light-analyte coupling and higher sensitivity. Moreover, at increasing

core porosities, the air pores enlarge, allowing more light to pass through the core and hence greater light contact with the sample. The highest sensitivity of 81.16% is obtained for 2THz with 98% porosity.

In Fig.6.3b, an overall effect on sensitivity w.r.t frequency has been detected for both kinds of milk, for example, cow and camel milk. The curves show that the sensitivities of cow and camel milk grow within the narrow spectrum of 0.2 to 1.6 THz, then begin to drop for the higher frequency of 1.6 THz to 2.0 THz. The first increase can be attributed to increased light-analyte coupling. Cow milk has a marginally greater relative sensitivity over camel milk because of its greater RI.

When the frequency is taken as 2 THz and the light has a wavelength lower than the core diameter between 260 μm and 400 μm, a modification in D_{core} has a smaller impact on the fiber's sensitivity as shown in fig6.3c. Thus light is completely contained within the region of the core, and the sensitivity is very slightly impacted by variations in diameter.
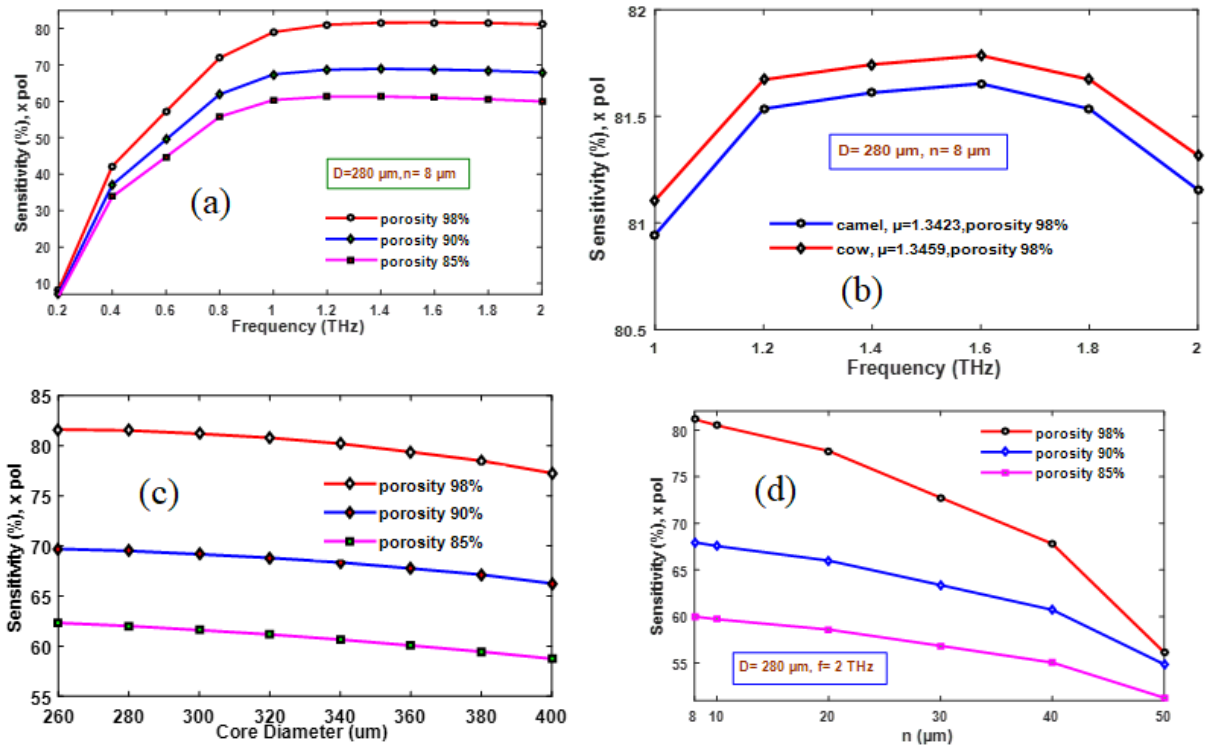
Fig 6.3: Sensitivity performance vs (a)frequency w.r.t porosity for cow milk, (b)frequency for cow and camel milk for 98% porosity, (c) core diameter w.r.t porosity for cow milk, (d) strut size w.r.t porosity for cow milk

The sensitivity percentage decreases as the strut size is increased from 8 to 50 micrometers, as shown in Fig.6.3d. When the strut size is constant at 8μm, the maximum sensitivities achieved are

81.16 percent, 67.96 percent, and 60 percent for respective 98 percent, 90 percent, and 85 percent porosities.

6.3.2 Core power fraction and EML analysis

Figure 6.4(a) depicts the proportion of power delivered via the suggested PCF's core air holes as frequency increases. An improvement in power fraction with progressive frequency shows that more light is transported via the core air vents, implying that the beam's strength is localized more inside the core. Moreover, the same figure presents the EML variations w.r.t frequencies at varying pore sizes. Camel milk, for example, has the lowest 0.033013 cm^{-1} EML for 98 percent porosity and 0.057901 cm^{-1} for 90 percent pore size at a 2 THz frequency.

EML fluctuations in terms of frequency are shown in Fig.6.4(b) at optimum porosity of 98 percent, 280µm core diameter, and 8µm strut. Background substance Zeonex traps more light as frequency rises, suggesting increased material loss. Furthermore, the trends are similar to what is observed in fig 6.3c for the core power fraction w.r.t core diameter in fig 6.4c.

In the case of constructing terahertz sensors, a greater core power percentage and a lesser EML are two essential attributes. The core power fraction decreases as the strut elongates, as shown in Fig.6.4d. In the case of 98 percent porosity, the core power fraction changes to 57.184 percent from 81.573 percent for changing from 8 to 50 micrometers of strut sizes. When the strut value is fixed at 8µm for both situations, the greatest values of 69.538 percent and 62.041 percent of core power fractions are attained for pore sizes of 90 percent and 85 percent. Because an increase in strut size denotes a rise in the quantity of background material employed, it contributes to greater effective material loss levels. The minimum quantities of EML are 0.033013 cm^{-1} for porosity of 98%, 0.057901 cm^{-1} for 90%, 0.073161 cm^{-1} for 85% keeping 8µm strut.
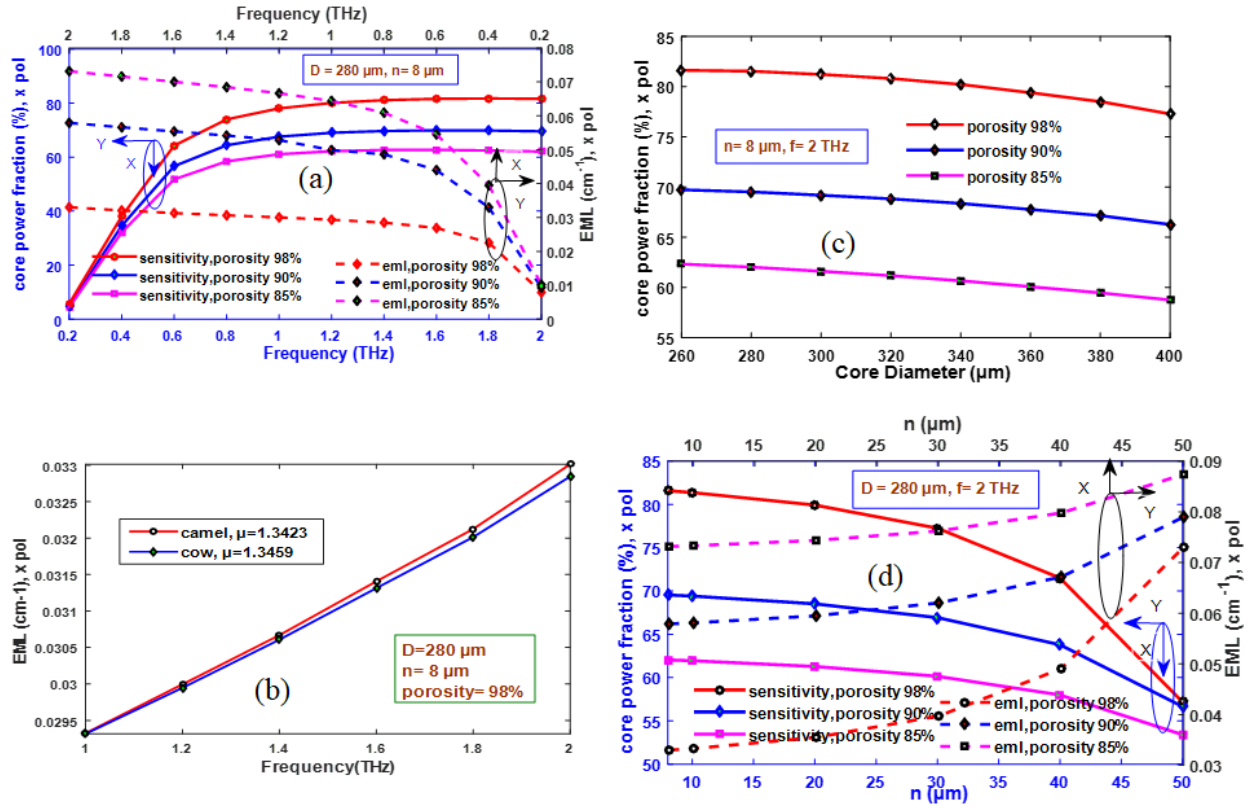
Fig 6.4: (a) core power fraction and EML vs frequency (b)EML w.r.t frequency (c) core power fraction vs D$_{core}$ (d) core power fraction and EML vs strut

6.3.3 Effective area analysis

The impacts on the effective area of different frequencies at varying pore sizes are displayed in Fig.6.5a, whilst a similar relationship is presented in Fig.6.5b, but for optimized structural parameters. As frequency increases, the light becomes highly restricted inside the core, reducing the effective cross-sectional region [34]. For the provided spectral region of 0.2 THz to 2 THz, the effective area of camel milk fluctuates from 4.97×10^{-6} m^2 to 9.38×10^{-8} m^2 with a pore size of 98 percent. Similarly, with a porosity of 90%, it moves from 4.92×10^{-6} m^2 to 8.74×10^{-8} m^2, and for a porosity of 85%, it shifts to 9×10^{-6} m^2 from 8.43×10^{-8} m^2. When at 2 THz as an analyte, cow milk is utilized, the minimum possible effective area of 9.30×10^{-8} m^2 is discovered.
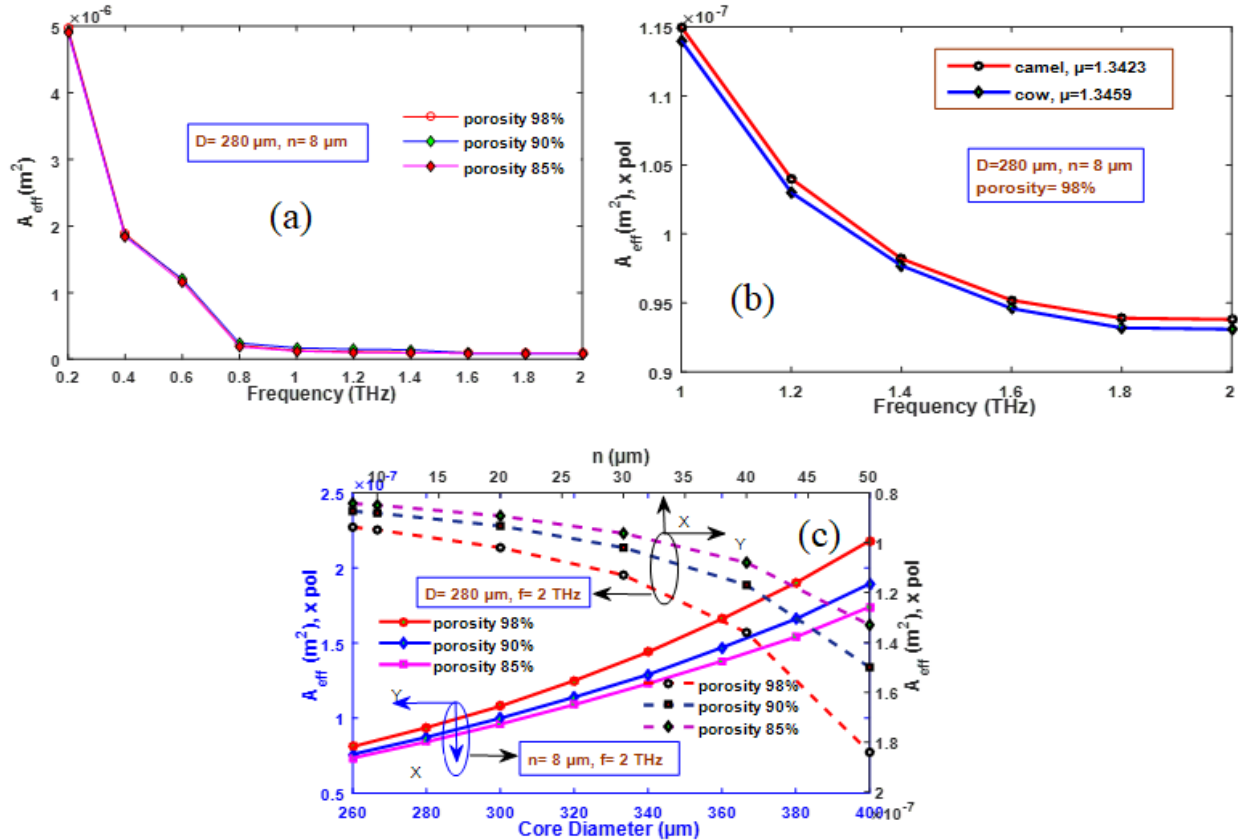
Fig 6.5: Effective area vs (a)frequency w.r.t porosity (b) frequency for 2 types of milk (c)core diameter and strut

When the pore size is retained at 98 percent for camel milk, the effective area has the lowest result of 8.11×10^{-8} m^2 and the highest amount of 2.18×10^{-7} m^2 for core dimensions of 260μm and 400μm, respectively in fig6.5c. In the same graph, increasing the strut size from 8 to 50 micrometers leads to a change in the effective area. As the strut length increases the effective area diminishes. For 85 percent, 90 percent, and 98 percent porosities, the strut measurement of 8μm has a minimal effective area of 8.43×10^{-8} m^2, 8.74×10^{-8} m^2, and 9.38×10^{-8} m^2.

6.3.4 Effective refractive index analysis

When the frequency increases to 2 THz from 0.2 THz for 98 percent porosity, the effective refractive index improves to 1.3492 in fig6.6a. This happens since more light can engage with the core's surrounding material for a greater frequency, causing a rise in the effective RI. The effective index is also affected by the pore size of the core, as a decrease in core porosity results in a higher background substance for the core, leading to increased light contact with Zeonex. Thus the effective index is obtained as the highest value of 1.3879 for 85 percent. As can be seen in Fig.7.6b, as the core diameter improves the effective refractive index expands. For 85 percent

porosity, the refractive index rises from 1.3881 to 1.3976, greater than for 90 percent and 95 percent porosity in the same figure.
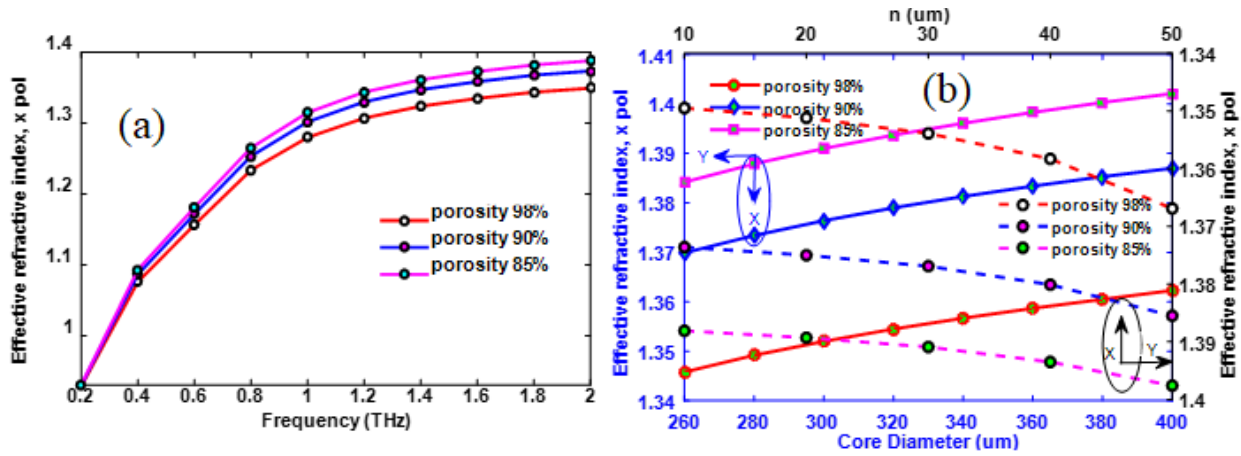
Fig 6.6: Effective refractive index vs (a) frequency w.r.t different porosities (b) core diameter and strut w.r.t various porosities

6.3.5 Numerical Aperture (NA) analysis

We can see in Fig.6.7a that as frequency increases, numerical aperture responds in an increasing pattern until 0.6 THz, then downhill until 2 THz. Formerly, it was discovered that even a small increase of 0.4 THz resulted in a significant drop in effective area. As a result, even though the frequency was increased, for 0.6THz the greatest NA was determined to be 0.55, and subsequently, the values began to fall as the effective area began to plateau for varying pore sizes. The modification of NA can also be seen by changing the strut, n, and core diameter separately while leaving the other factors constant in fig6.7b. Both measurements display that NA is falling, which is not good for a sensor. As a result, we can deduce that the optimal values should be = 280 m and n = 8 m, respectively, as previously determined.
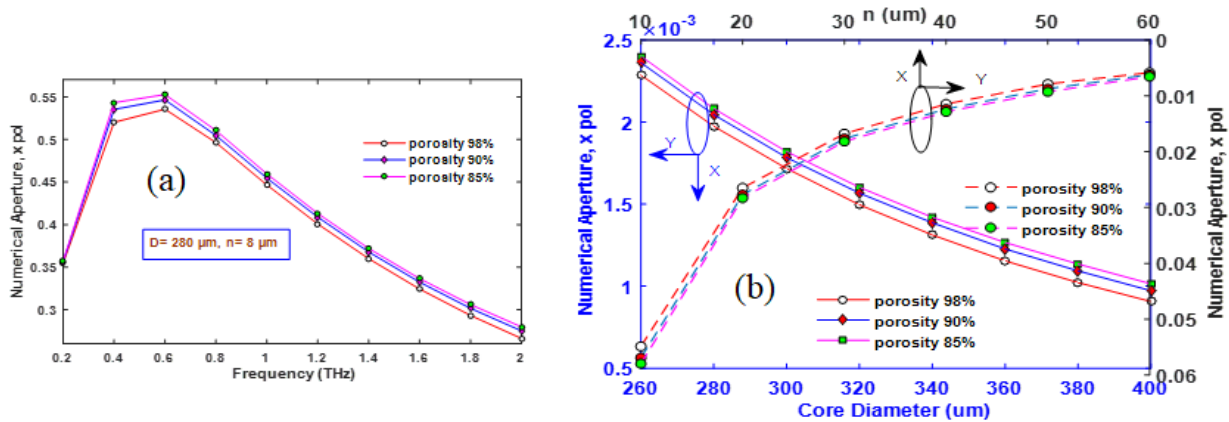
Fig 6.7: NA vs (a) frequency w.r.t porosity, (b) core diameter and strut size w.r.t. porosity for x-pol

27

6.3.6 Confinement loss and dispersion analysis

For camel milk, the characteristic of confinement loss is examined by adjusting the frequency values between 0.2 THz and 2 THz. A better concentration of light in the core occurs as the light becomes highly restricted inside the core at a greater frequency. As a result, the confinement loss graph in Fig.6.8a displays a decreasing trend with higher frequency. The dispersion curve in Fig.6.8b indicates a declining trend as frequency expands. It happens as a result of reduced RI variance occurring at a higher frequency. The readings are nearly identical for varied pore sizes. It is seen that dispersion flattens out in the spectra of 0.8 THz to 2 THz. In several communication applications, the broader flatter spectrum performs better. For any porosities, the proposed design achieves 1±0.5ps/THz/cm dispersion at the optimized architectural parameters.
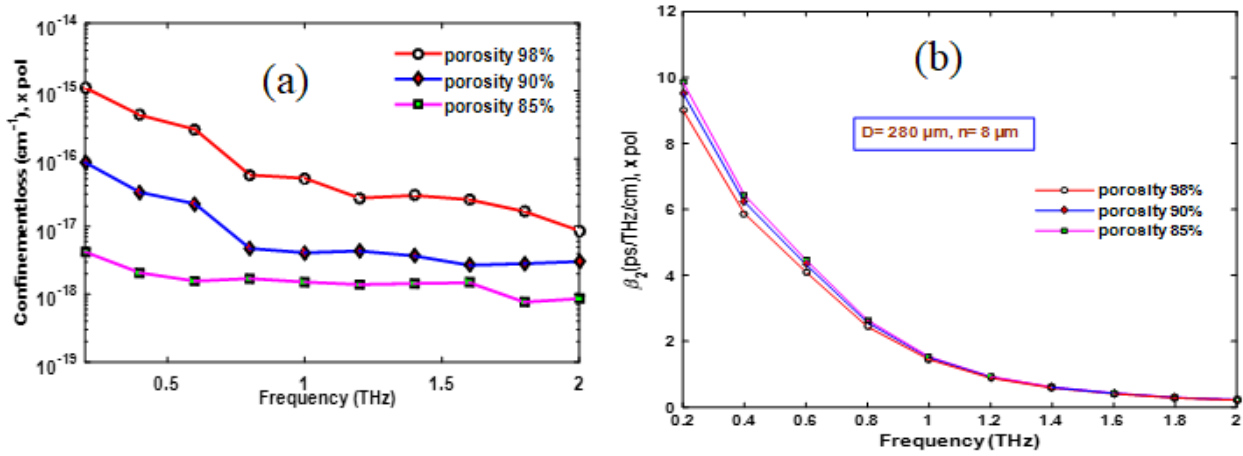
Fig 6.8: (a) confinement loss vs frequency (b) dispersion vs frequency

6.4 Comparison analysis

Table 6.1: Evaluation of the suggested sensor's performance parameters to some of the previous works

References	EML (cm^{-1})	Max Sensitivity	Confinement Loss	Dispersion ps/THz /cm	Numerical aperture
[35]	0.07	-	1.14×10^{-3} cm^{-1}	1.1 ± 0.02	-
[36]	0.035	-	$6.3\times10^{-3}cm^{-1}$	0.46 ± 0.07	-
[15]	-	80.93%	1.23×10^{-11} dB/cm	3.32 ± 1.82	-
[37]	-	49.13%	5.583×10^{-5} dB/m	-	-

[38]	-	85.7%	1.7×10^{-7}cm^{-1}	-	0.372
[34]	0.05	-	7.24×10^{-7} cm^{-1}	0.49±0.05	-
Proffered design (Camel milk)	0.033	81.16%	8.675×10^{-18} cm^{-1}	1±0.5	0.256
Proffered design (Cow milk)	0.032824	81.32%	1.435×10^{-18} cm^{-1}	1±0.5	0.267

6.5 Conclusion

This chapter proposes a PCF sensor based on wheel shape structure with Zeonex having a porous core for detecting cow and camel milk to operate in the THz spectral range. This work analyzes and discusses sensing characteristics employing the finite element (FEM) method. The largest sensitivity values are 60%, 67.96%, and 81.16% for consecutive porosities of 85%, 90%, 98% having a small EML of 0.033 cm^{-1}. This PCF sensor also has a significant 81.573 percent of core power fraction, a superior 0.256 for numerical aperture, and a smoothed dispersion across a wideband. With all of these benefits, it is reasonable to conclude that this biosensor will pave a new direction in the dairy sector and will assist in the quality assurance of dairy foods.

Chapter 7

Proffered design 02-Quadrature cluster-based SPR-PCF for multidimensional applications with greater figure of merit

7.1 Introduction

Analyte identification based on surface plasmon resonance (SPR) has introduced a new dimension to optical sensing technology, with applications in biomedical research, bio-imaging, pathological testing, and other domains. The evanescent field that enters the sensor causes electrons to oscillate at the interface of a plasmonic substance, resulting in surface plasmon waves (SPW). Because of the absorption of light going through the fiber, the SPR phenomenon occurs when the frequencies of this EM wave and the SPW are synchronized, resulting in a resonance spike. This resonance peak can shift because of the slight fluctuations in the analyte's RI. The design performance can be increased by adjusting two key factors, structural characteristics and the sensor's calibration. This chapter offers a highly sensitive SPR-based PCF for detecting unspecified solutes with varied RI with an exceedingly high figure of merit. This sensor can also be used to analyze RI alterations of an analyte caused by temperature and magnetic field fluctuations. As a result, it can serve as a versatile sensor. To improve the fiber's sensor performance, a combo of Au-TiO$_2$ coatings was employed to induce increased SPR excitation. Four tiny air pores are deliberately positioned in between the clustered cladding zone to diminish the CL values. The functionality of the device is then evaluated by adjusting the thickness of the bimetallic layer, pitch, and the air holes' diameter in conjunction with fabrication capabilities.

7.2 Geometrical structure and field distribution

Fig7.1 shows the 2D cross-sectional image of the suggested fiber. The suggested structure was created using the COMSOL Multiphysics v5.3a like the previous chapter. In the cladding layer, the fiber's lattice is made up of four bunches of small holes made of d$_1$ diameter. Five round holes are located vertically in one pair of clusters, while four circular air gaps are placed in a horizontal location in the other pairing. A fiber's guiding qualities and sensing behavior can be impacted by the structure and positioning of air holes. This cluster structure was made to reduce the fabrication challenges. The electromagnetic wave is deflected and guided from the core to the plasmonic metal through four channels that are 90 degrees apart. The dispersity between the nuclei of any consecutive air vents is known as pitch. Tiny holes can be inserted into the channels to diminish the light leakage coming from the core. Thus between the four clusters, four tiny air pores with a diameter, d$_c$ of 0.2 μm are inserted into the cladding. A PML with t$_p$ = 1.50 μm thickness is deposited on the exterior of the surface. This coating aids in the absorption of the evanescent field that is radiated. The external sensing technique is employed in this design. This layer that is

introduced to use this technique is mostly utilized to detect undiscovered mixtures with varying RI with a constant thickness $t_a = 1.20$ μm. As a plasmonic layer, a thin coating of gold (Au) is placed underneath the analyte coating to generate a large number of plasmons.
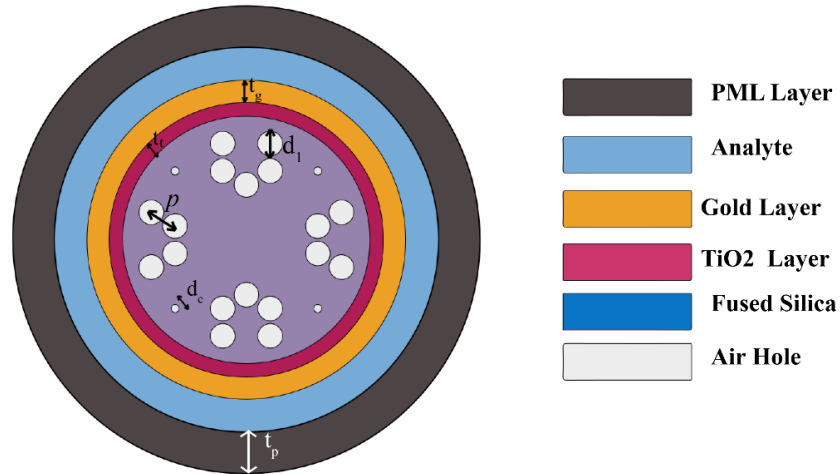
Fig 7.1: Cross-sectional view of QC-SPR-PCF

(a)   (b)   (c)   (d)
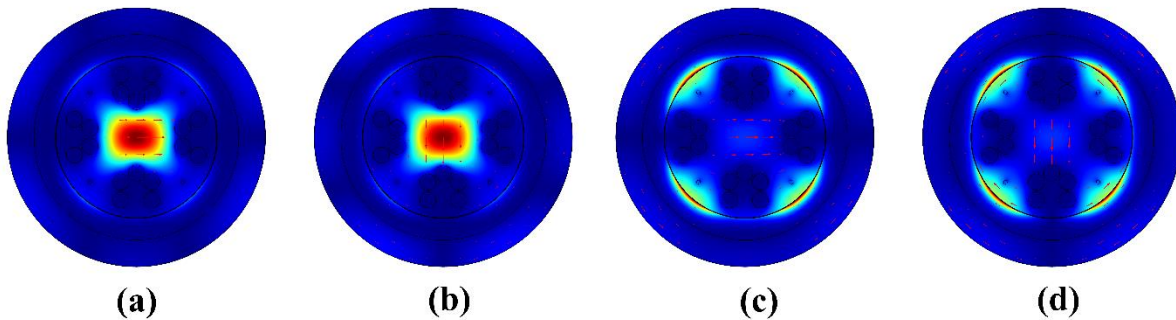
Fig 7.2: Field distribution of core mode (a) x-pol, (b) y-pol and SPP mode (c) x-pol, (d)y-pol

Due to the coupling of the gold material with the evanescent field, the interaction of the core mode with SPP mode as shown in **Figure.7.2** develops in resonance, hence the SPR phenomenon [39]. The wavelength of resonance and the peak amplitude of the loss spectrum are two significant criteria that largely depend on the sample under inquiry. The loss peak fluctuates in response to changes in the RI. As a result, each specimen has a separate CL peak at a particular resonant frequency. At both the x-directional modes, for RI = 1.37, the dispersion relationship of SPP and core mode at the pairing phase is depicted in Fig.7.3. The real effective index of these two modes coincides at an RW of 0.63 μm, demonstrating an 11.012 dB/cm confinement loss.
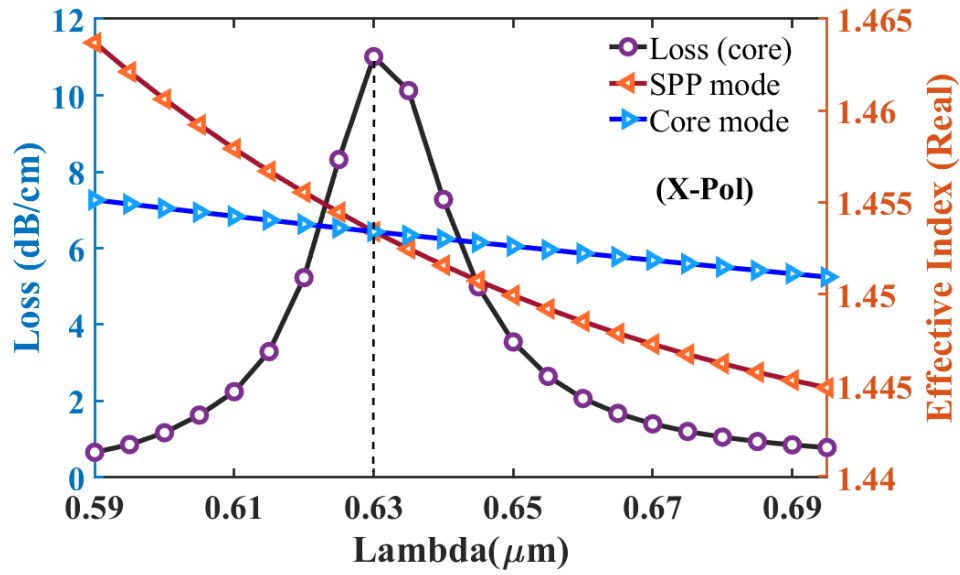
Fig 7.3: Dispersion property of the core and SPP mode and loss graph for RI 1.37

7.3 Optimization of structural parameters

7.3.1 Bimetallic Layer (Au-TiO2) Thickness

The thickness of Au-TiO$_2$ layers is critical to the sensor's performance. Changes in each of these parameters can cause the RW and loss peaks to vary. Here the changes in x-pol modes are explained because of their higher losses than that of y-pol.

Figure 7.4 (a) shows that increasing the thickness of gold to 25 nm from 15nm pushes the peak of the losses to the right side and enhances the RW values. For RI of 1.37, when the gold thicknesses are 15 nm, 20 nm, and 25 nm, the CL values are 10.650 dB/cm, 11.580 dB/cm, and 11.010 dB/cm whereas n_a = 1.38 provides the values of 14.637 dB/cm, 15.815 dB/cm, and 14.567 dB/cm, respectively. Moreover, the highest AS value of 805.782 RIU^{-1} is achieved for 20nm thickness in figure 7.4b and thus, it is considered the optimized value for further investigation. For both RI 1.37 and 1.38 analytes, the highest loss values are obtained for 15 nm thickness. For RI = 1.37, TiO$_2$ thickness of 5 nm, 10 nm, and 15 nm provides the consecutive CL peaks of 10.238 dB/cm, 11.580 dB/cm, and 12.989 dB/cm and 14.194 dB/cm, 15.815 dB/cm, and 17.709 dB/cm for RI = 1.38 in fig 7.5a. The greatest AS of 805.782 RIU^{-1} is obtained at a layer thickness of 10 nm, as shown in Fig.7.5 (b). Furthermore, when contrasted to the loss acquired at 15 nm, the loss is reduced. As a result, t_t = 10 nm is selected as the optimal thickness of TiO$_2$, considering both the values of CL and the high sensitivity.
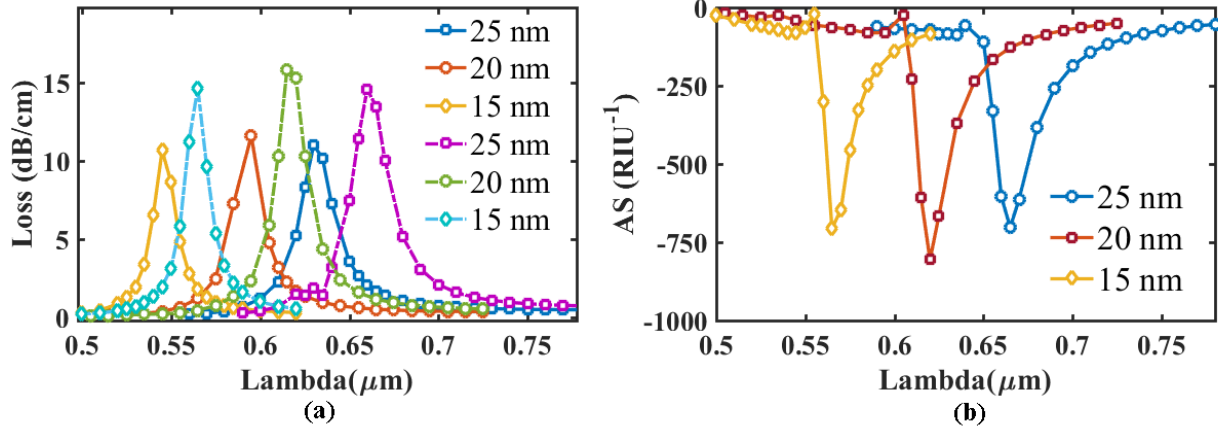
Fig 7.4: (a) CL vs wavelength (b) AS vs for variation of gold thickness for 1.37 RI (solid line) and 1.38 RI (dotted line)
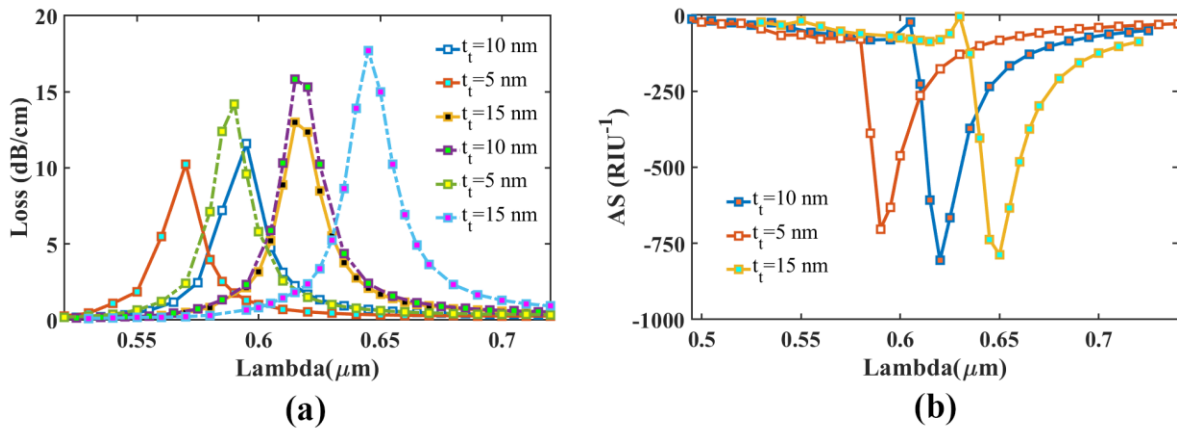
Fig 7.5: (a) CL vs wavelength (b) AS vs wavelength for variation of TiO2 thickness for 1.37 RI (solid line) and 1.38 RI (dotted line)

7.3.2 Regular air hole diameter d1 and Pitch p

The diameter of the round air holes that formed the four clusters has a substantial effect on the fiber's sensing response. At RI of 1.37 and 1.38, diameter d_1 has been reduced from 0.90 µm to 0.85 µm, leading to a rise in CL, as seen in Fig.7.6(a). Nevertheless, as demonstrated in Figure 7.6 (b), AS reduces as the diameter diminishes. When the diameter is improved to 0.95 µm, the amplitude sensitivity is boosted to 817.338 RIU^{-1}, with a CL of 10.1291 dB/cm for 1.37 RI and 13.20773 dB/cm at a refractive index of 1.38.

The spacing between the nuclei of any consecutive air holes, referred to as pitch, has a significant impact on the AS and CL of the device. It's worth noting that variations in pitch do not affect resonance wavelength quantities. The pitch was set at 1 µm and subsequently enhanced to 1.05 µm to observe how it affected the analytes' loss and sensitivity values. A pitch of less than 1 µm was

avoided because it would result in an overlay of the air holes, which have been calibrated at 0.95μm.
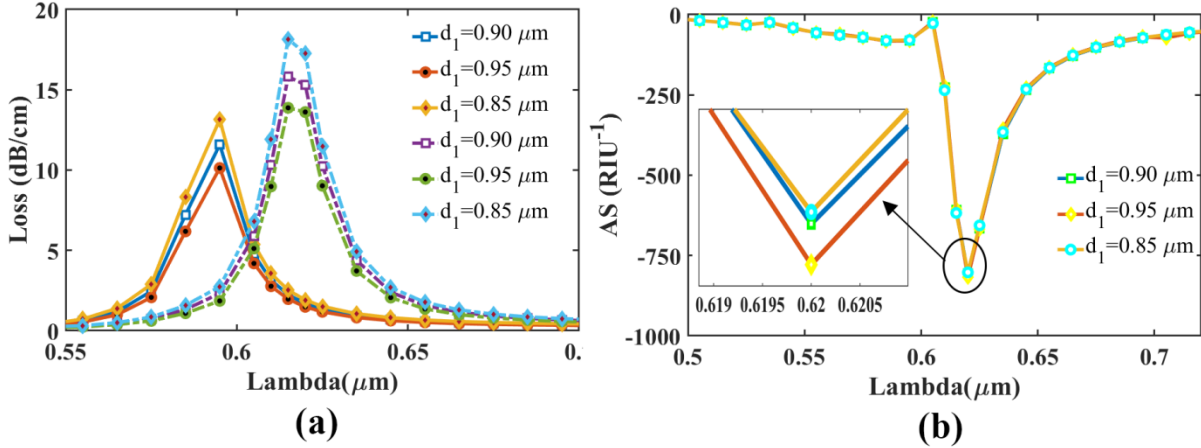
Fig 7.6: (a) CL vs wavelength (b) AS vs wavelength for variation of regular air hole thickness for 1.37 RI (solid line) and 1.38 RI (dotted line)
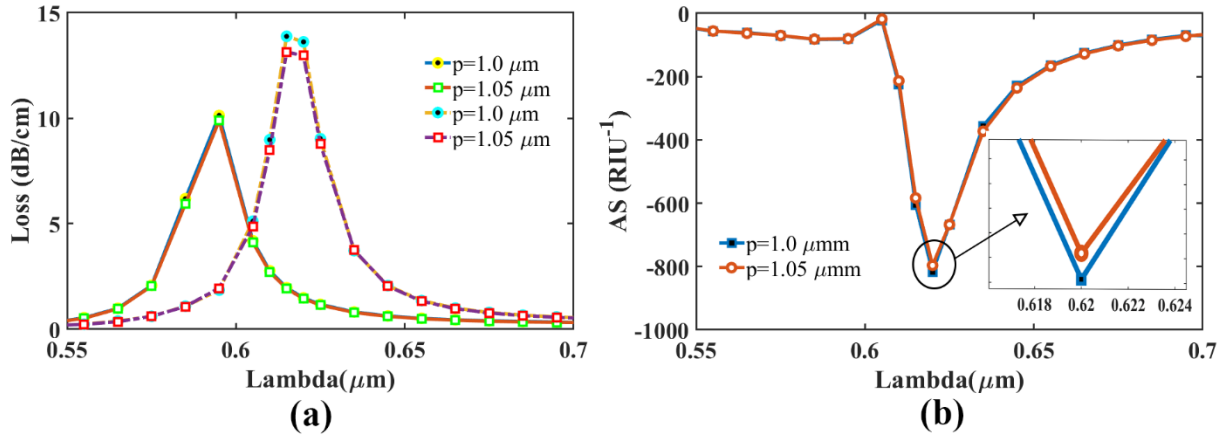
Fig 7.7: (a) CL vs wavelength (b) AS vs wavelength for variation of the pitch for 1.37 RI (solid line) and 1.38 RI (dotted line)

As can be seen in figure 7.7a, increasing the pitch separation causes the air holes to fill more area, which enhances light concentration and minimizes losses. However, as displayed in Figure 7.7b, the AS decreases as the pitch size is improved from 1 μm to 1.05 μm. (b). Finally, because of the overall high sensitivity, a pitch of 1 μm is preferred.

7.4 Multidimensional Applications

7.4.1 RI sensor

To evaluate the suggested sensor, the CL and AS of numerous analytes are investigated for diverse RI values. The parameters of t_t, t_g, d_1 and p are preserved at their most optimal for evaluating the RI of the sample, ranging from 1.32 to 1.43. The shift of core-guided and SPP modes' phase-matching position of wavelength occurs with the change of their RI's real part due to RI variability. When less energy transmits from core to SPP mode, the right shift in RW is noticed for greater analyte RI [40]. The resonance wavelength for the x-pol mode varies from 0.525μm to 1.49μm, whereas the RW for y-polarization grows from 0.525 μm to 1.62 μm, as depicted in Figure 7.8(a-b). A substantial variation in CL values can be seen owing to the discrepancy in resonant wavelength. The maximum WS of 61500 nm/RIU for x-pol and 75000 nm/RIU for y pol is attained because of the RW's shift from 1.42 to 1.43.
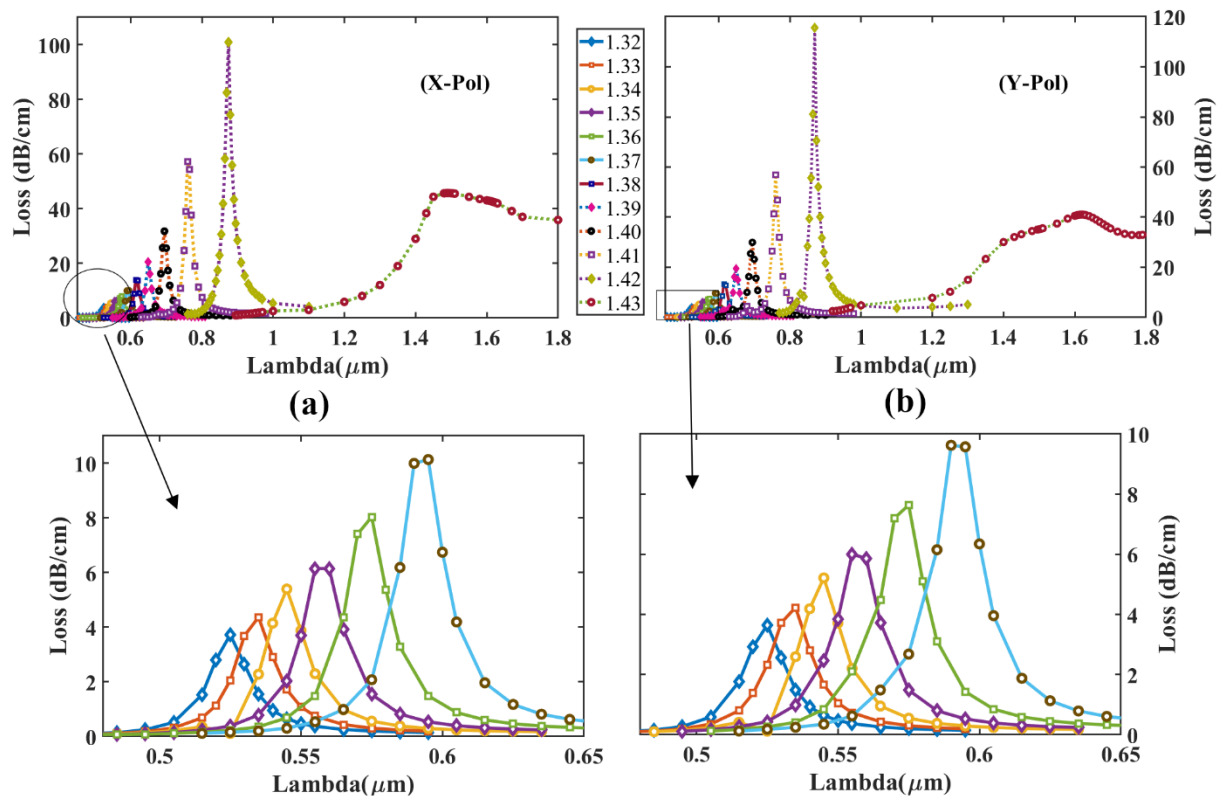
Fig 7.8: Loss vs wavelength for the variation of RI in (a) x-pol (b) y-pol

Because of the peak adjustment of confinement loss for numerous RI, for x-pol, the associated AS values increases from 205.46 RIU^{-1} to 4419.6 RIU^{-1} and 201.1 RIU^{-1} to 5274 RIU^{-1} for y-pol when RI is shifted from 1.32 to 1.41 in Figure 7.9(a, b). The AS quantities for RI 1.42 decrease dramatically for both modes. The reason for this is that when RI is 1.43, for x-pol, the CL peak lowers to 45.71 dB/cm and for y-pol, it is 41.02 dB/cm. As a result, we've preserved our AS inquiry

up to 1.42 RI. X-pol has a maximum AS of 4419.62 RIU^{-1} for RI 1.41, and y-pol exhibits the highest value of 5274 RIU^{-1}.
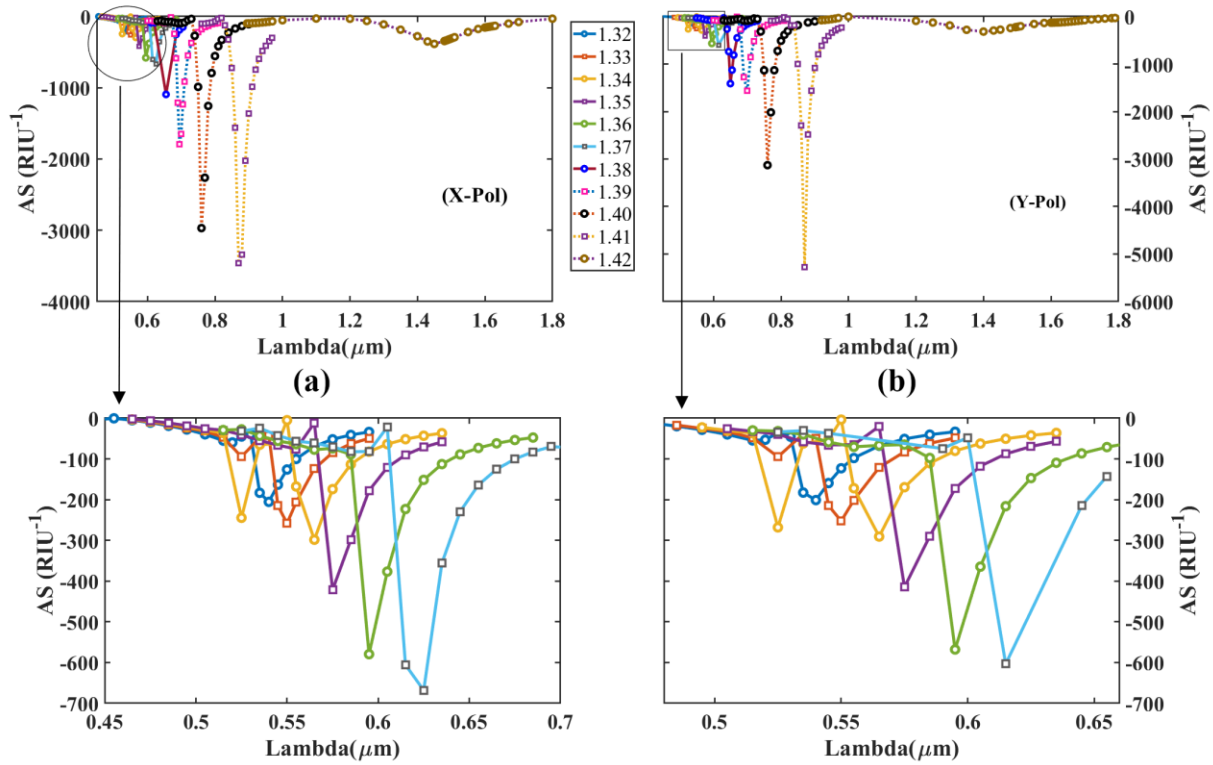
Fig 7.9: AS vs wavelength variation of RI in (a) x-pol (b) y-pol

7.4.2 Temperature sensor

All of the preceding experiments were conducted at a constant temperature. Meanwhile, in the real world, the atmosphere, hence the temperature, can change with time. To make our system further interactive, we intended to measure its sensitivity w.r.t temperature putting ethanol as a sample analyte. Assessing ethanol's the boiling (78.37°C) point and melting point (114.1°C), we set our detectability within -70°C to 70°C. The equivalent qualities of fused silica are sufficient (melting point 1660°C - 1710°C, boiling point 4046°C) that temperature difference within this region does not affect the sensor performance [20]. In Fig. 8.10a, the RW shifts from 550 to 650 nm, with the lowest CL value of 5.39 dB/cm for 70°C and the highest 20.6 dB/cm value for -70°C. Figure 7.10b shows the polynomial curve of RW for this specific temperature scale. It reveals a noteworthy value of $R^2 = 0.99929$ for the coefficient, which fits the detection capability. The sensor has an optimum sensitivity of 1 nm/°C and an average of 0.71 nm/°C sensitivity. It has a resolution of 0.1 degrees Celsius w.r.t temperature.
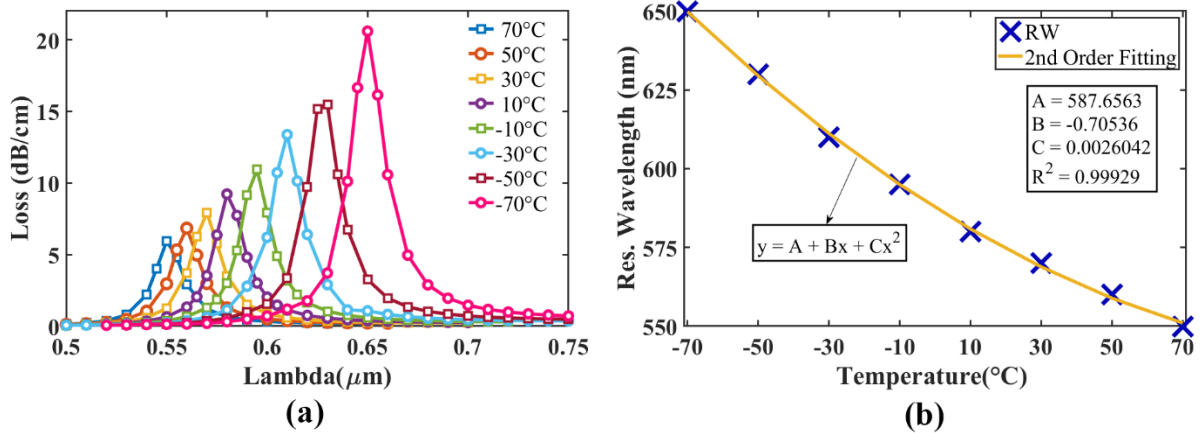
Fig 7.10: (a) CL vs wavelength (b) polynomial behavior for varying temperature.

7.4.3 Magnetic Field Strength (MFS) Sensor

The provided design can be employed as an MFS sensor in addition to monitoring the analyte's refractive index and serving as a sensor for identifying temperature. For this study, we used a magnetic fluid with a refractive index that is altered due to the variation of the magnetic field and temperature. Because of the development of RI, the RW changes to 625 nm from 535nm, and the CL peak increases from 4.6 dB/cm to 15.9 dB/cm, as shown in Figure 7.11(a) and 160 pm/Oe is the greatest sensitivity for this investigation. With the highest resolution of 0.625 Oe, 90 pm/Oe is the average value for magnetic sensitivity. The 2nd order polynomial fitting of RW w.r.t MFS is depicted in Figure 7.11 (b) and a high $R^2 = 0.99741$ is obtained.
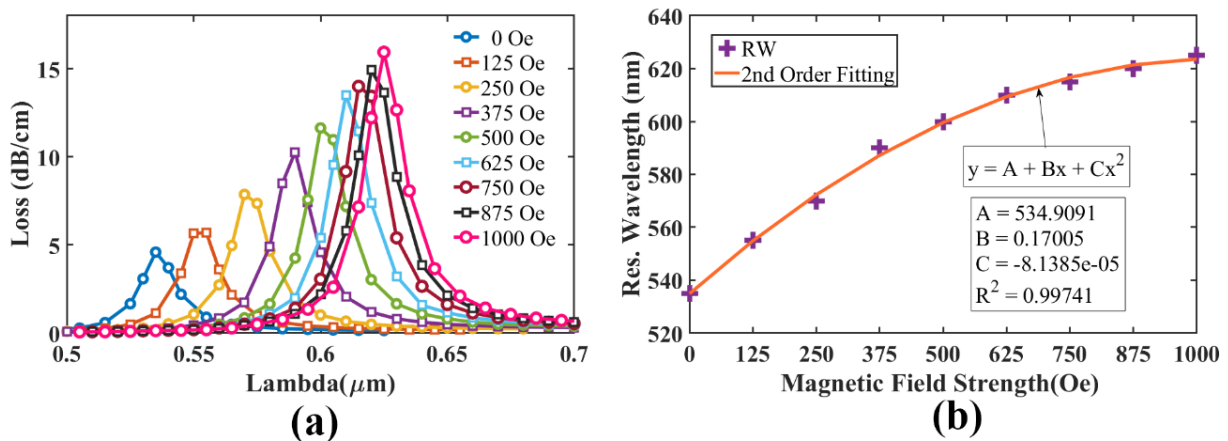
Fig 7.11: (a) CL vs wavelength (b) polynomial behavior for variation of magnetic field strength.

7.5 Comparison Analysis

Table 7.1: Evaluation of the suggested sensor's performance parameters to some of the previous works

Reference	RI range	Max AS (RIU^{-1})	Max WS (nm/RIU)	Amplitude Resolution (RIU)	Wavelength Resolution (RIU)	FOM (RIU^{-1})	Temp. sensitivity (nm/°C)	Magnetism Sensitivity (pm/Oe)
[41]	1.47-1.48	700	8,000	1.78×10^{-5}	1.25×10^{-5}	138	---	---
[42]	1.33-1.345	---	---	---	---	---	-1.81 (20°C to 60°C)	---
[43]	1.33-1.42	4358.09	21000	2.29×10^{-6}	4.76×10^{-6}	729	---	---
[22]	1.43-1.45	---	4,755	---	---	---	---	61.25(50Oe to 130 Oe)
[5]	1.33-1.41	5000	32,500	2.00×10^{-6}	3.08×10^{-6}	448	---	---
[17]	1.33-1.38	1411	25,000	---	4.00×10^{-6}	502	---	---
[44]	1.35	---	---	---	---	---	0.72 (0°C to 100°C)	---
[20]	1.32-1.43	5060	41,500	1.98×10^{-6}	2.41×10^{-6}	1068.7	0.75 (-70°C to 70°C)	---
This work	1.32-1.43	5274	75,000	1.90×10^{-6}	1.33×10^{-6}	4230.42	1 (-70°C to 70°C)	160 (0 Oe to 1000 Oe)

7.6 Conclusion

This chapter describes a PCF-SPR sensor for refractive index sensing, additionally used as a magnetic field strength (MFS) and temperature sensor, and claims that it can be a preferable alternative for sensing unspecified analyte over a wider RI span of 1.32-1.43. The plasmonic effect is improved by the air-gap clusters and the outer Au-TiO2 layer, which results in superior AS, WS, and FOM. For AS and WS, the highest values of 5274 RIU^{-1} and 75,000 nm/RIU, respectively, as well as a fantastic FOM of 4230.42 RIU-1 can be found. Furthermore, it has the highest 1 nm/°C of temperature sensitivity and the greatest 160 pm/Oe of MFS sensitivity. After evaluating our findings with those of previous studies, we observed that this design is a better contender for all the performing criteria. As a result, for a large RI range of substances, our suggested sensor would provide remarkable sensing properties in bio-sensing and pharmaceuticals.

Chapter 8

Proposed design -03: LSPR based double peak double plasmonic layered bent core PCF-SPR sensor for ultra-broadband dual peak sensing

8.1 Introduction

This chapter proposes a LSPR based sensor. The combination of two different plasmonic materials produced a novel dispersion relation with double resonance peaks. When AZO is utilized as the middle plasmonic material, the simulated results show that this sensor has a maximum amplitude sensitivity of 8485.2 RIU^{-1} along with a maximum spectral sensitivity of 46300 RIU/nm in y-polarization. A higher figure of merit of 2923.2 can be attained, suggesting that this sensor has a greater detection accuracy and maximum linearity of R^2 = 0.99312. Furthermore, the proposed sensor has its ability to detect unidentified analytes with refracting indexes ranging from 1.27 to 1.45. A new sensitivity parameter called double peak shift sensitivity has been proposed in this study, in addition to the sensitivity parameters derived from studying the double peaks independently. When evaluating the double peaks together for two adjacent RIs, this sensor has a maximum double peak shift sensitivity of 4400 RIU/nm and 16500 RIU/nm for x-polarization mode and y-polarization mode respectively. Furthermore, the proffered sensor is a promising contender for "Quantum Entanglement"-based research works.

8.2 Sensor structure

Figure 1 depicts a two-dimensional cross-sectional view of the proposed sensor's geometrical structure. This structural pattern was created with the help of COMSOL Multiphysics 5.3a program. From Fig.1, it can be seen that the unidentified analyte layer, as well as PML (Perfectly Matched layer), are outside of the cladding zone for external sensing. Just beneath the analyte layer, three different plasmonic layers with gold and AZO as plasmonic materials are arranged in a precise order. Gold was chosen for its chemical stability and non-reactivity, whereas AZO was chosen for its operational frequency zone, where evanescent waves penetrate deeper[43]. The cladding region is made up of two rings of circular air holes, twelve of which are hexagonal-shaped rings and three of which are triangular-shaped circles. The radius of larger air holes is represented by r_2, whereas the radius of small air holes is represented by r_1. The larger air holes are placed in such a way that light may be confined more tightly in the core, reducing confinement loss. Silica in the fused form is utilized as background material. Small air holes are positioned towards the three distinct plasmonic layers in figure 8.1.
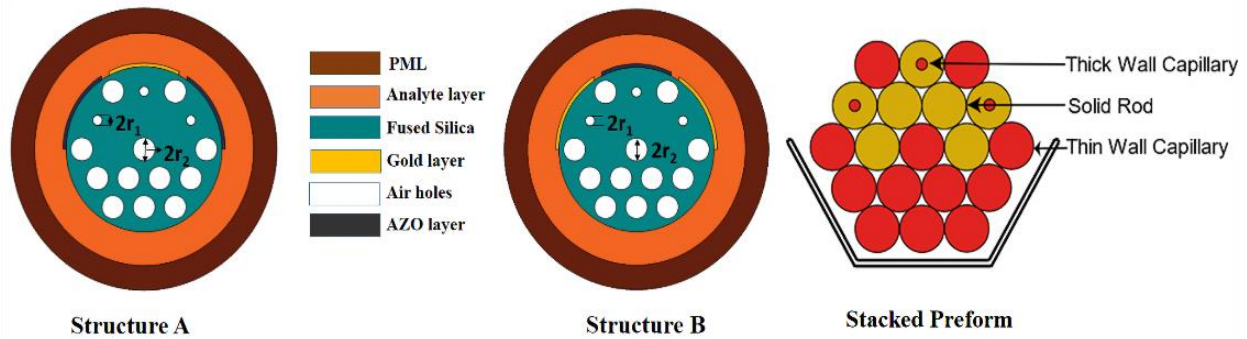
Figure 8.1. Cross-sectional structural design of the sensors provided (Structures A and B) and a diagram of stacked preforms for manufacturing the sensors

8.3 Optimization of structural parameters

Using the finite element method, we study the effect of AZO and gold placement on different structures A and B, and the effect of the thickness of the plasmonic layer and the radius of the circular air holes of different sizes on the detection capability. This sensor with the help of COMSOL Multiphysics 5.3a.Then optimization is done to get the best possible performance of the given sensor is done.
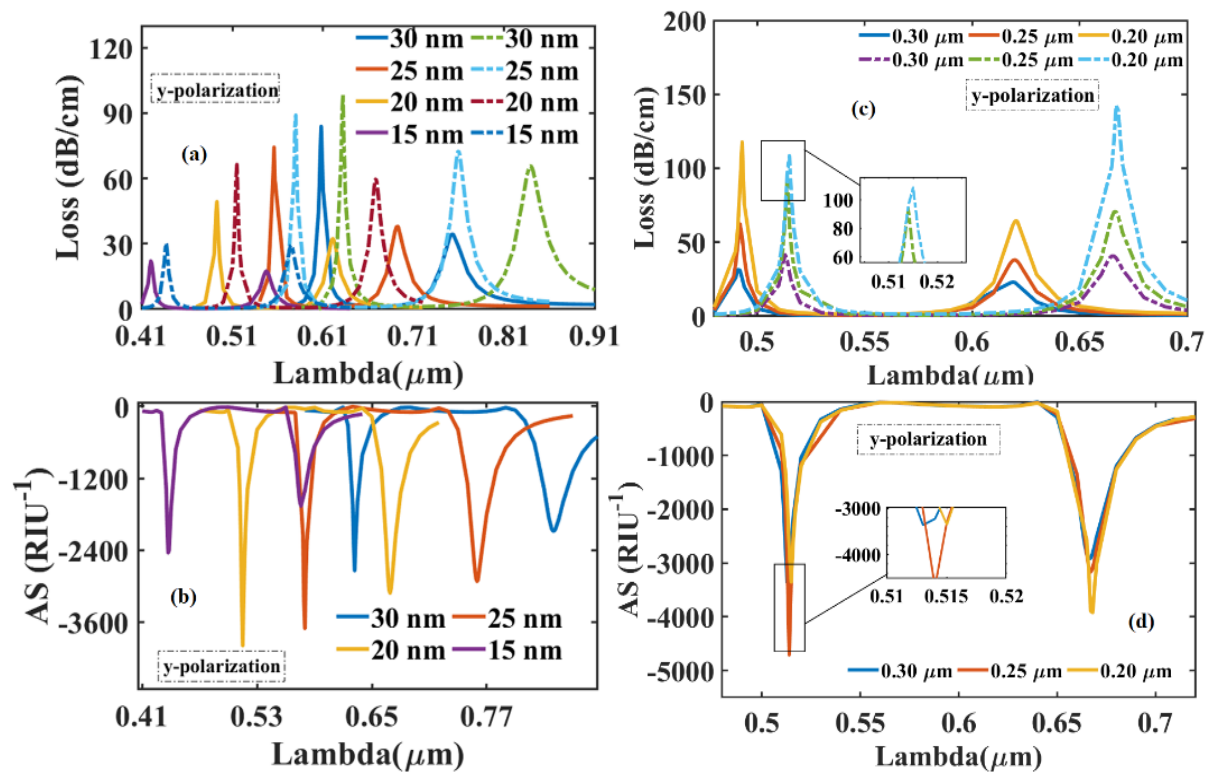
Figure 8.2. Effect of changes in AZO thickness and small hole radius on (a) and (c) inclusion loss and (b) and (d) fiber AS of the objects analyzed with RI 1.40 and 1.41 (structure) B)

8.3.1 Thickness of gold and AZO layer

It can be assessed from Fig. 8.2 (a) and (b) for structure B that the resonance wavelength rises with an increament in the layer thickness for both peaks. As seen in Fig. 8.2 (b), the amplitude sensitivity (AS) rises as the AZO width was incremented from 15 nm to 20 nm due to increased confinement loss in the fiber. A 20 nm of AZO (y-pol) displayed low losses of 49.35 dB/cm and 66.39 dB/cm for the first peaks in Fig. 8.2. (a), but a maximum sensitivity of 4000.23 RIU^{-1}; hence it was chosen as the most favorable thickness. Similarly, 20 nm gold (for X-polarization of structure A) was selected for the maximum sensitivity value of 3704.094 RIU^{-1}.

8.3.2 Radii of different air holes

Structures A and B containing the analytes of RI 1.40 and 1.41 were analyzed for a small air hole radius r_1. The radius has changed between the initial values of 0.3 μm and 0.2 μm for both arrangements. The loss and amplitude sensitivity (AS) curves show better results and are only shown for y polarization. As can be seen in Figure 8.2 (c), reducing the radius from 0.3 μm to 0.2 μm increases the confinement .Therefore, 0.25 μm was selected to provide maximum amplitude sensitivity 4706.43 RIU^{-1} with the most robust coupling with fairly good losses of 62.37 dB / cm and 94.03 dB / cm at the first peak, as shown in Figure 8.2 (c) and 2(d).
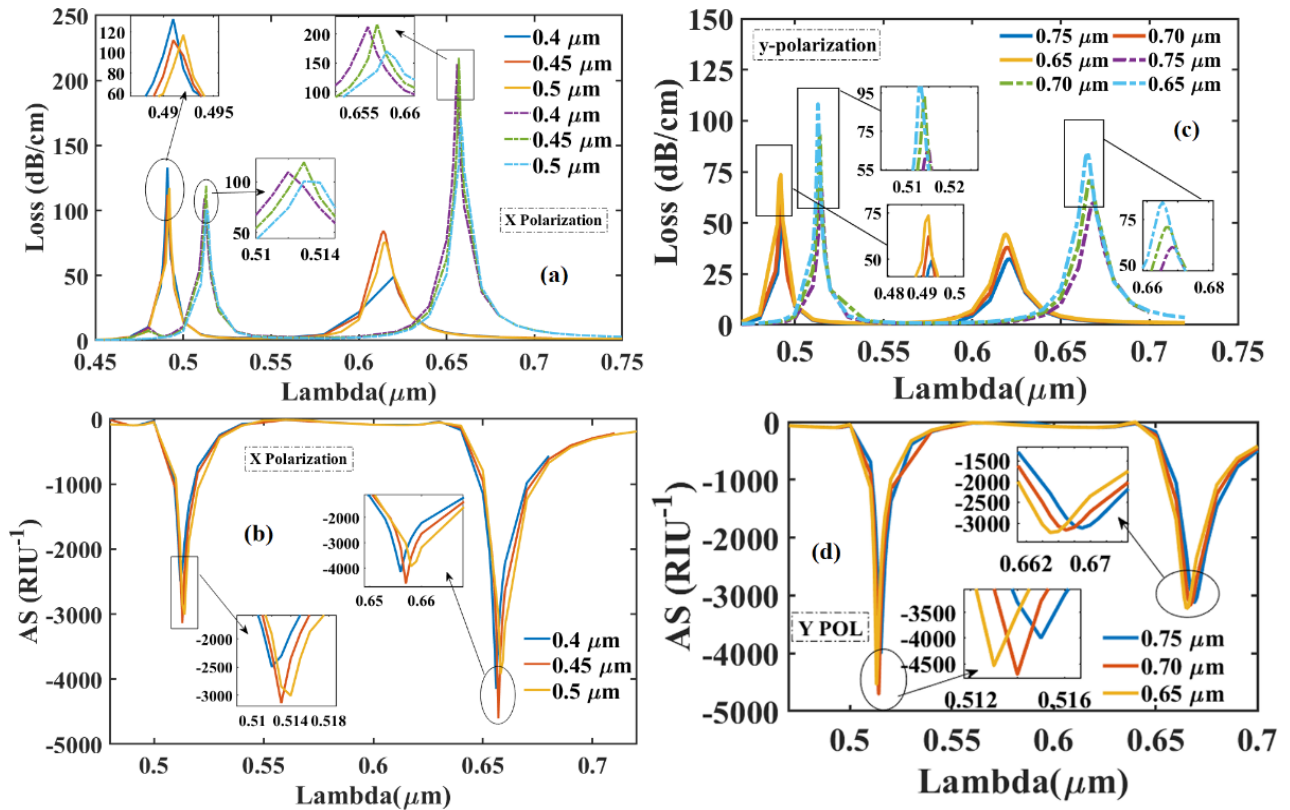
Fig. 8.3. Effect of the variations in radius of big air holes on (a), (c) loss, and (b), (d) AS for gold (structure A) and AZO (structure B), respectively

8.4 Features of the proffered sensor

8.4.1 Double phase-matching condition

The effective index of refraction in core guide mode and SPP mode is the same at certain wavelengths, producing the maximum light trapped in the fiber. Resonance occurs here, reaching the peak of large inclusion loss. The SPR-PCF sensor has two plasmonic materials, gold and AZO, that work at the same time, splitting the evanescent field into two, creating two different SPP modes, one for each material.Therefore, two different phase matching conditions and peaks can be observed at two non-identical resonant wavelengths in both x-polarized mode and y-polarized mode. With X polarization, AZO contributes to the first loss peak and gold contributes to the second loss peak as displayed in **figure 8.4.** Dispersion relations between core guide mode (purple line) and SPP mode (yellow and orange lines), showing maximum loss peaks of 72.986 dB / cm and 27.82 dB / cm at wavelengths 0.449 μm and 0.547 μm for each of the analytes with X polarization and RI of 1.41. The electromagnetic field distribution is also attached there where A and C represent core mode and B and D represent spp mode.
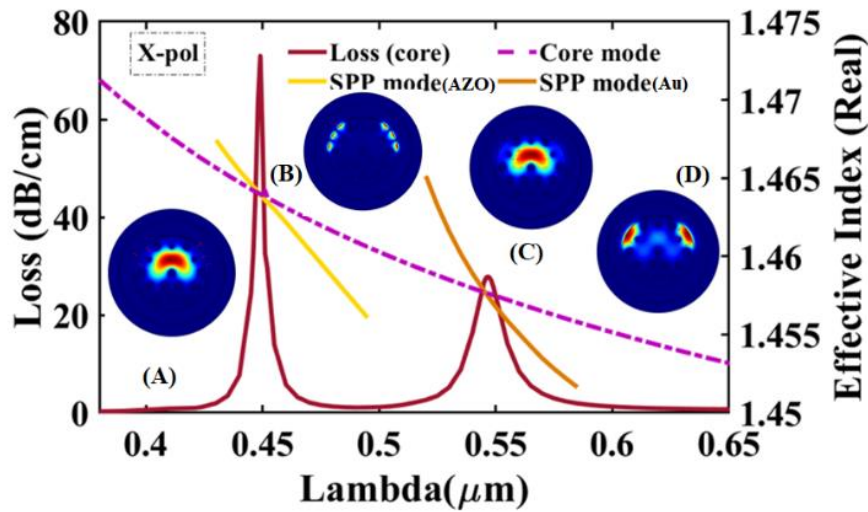
Fig. 8.4. Double peaks depicting the confinement loss and dispersion relation of the core mode (A) and (C) and two SPP modes (B) and (D) for an analyte RI = 1.41 for structure A

8.4.2 Detection of wide range of analyte RIs

Our sensors can detect a wide range of refractive index analysts from 1.27 to 1.41 in the xpol wavelength range of 360 nm to 750 nm and 1.27 to 1.45 in the ypol wavelength range of 370 nm to 1700 nm. The above refractive index confinement loss was investigated.

The loss trajectories in Fig 8.5 are red-shifted as RI increases, such as each peaks in every case. As the analyte's refractive index gradually increases, it's far in all likelihood to approach the value of the refractive index of the cladding vicinity submerged in fused silica. As the distinction among

the center and cladding quantities is reduced, coupling among them improves. Due to the deduction of propagation factors, the powerful mode index has a tendency to fall with the refractive index, prompting the center and SPP modes to converge at longer wavelengths.

8.4.3 Maximum Amplitude Sensitivity

For the practical implementation of a sensor, at first, a light source (i.e., HL-2000-LL, ocean optics) needs to be coupled with the fiber, surrounded by a target analyte[45]. Then, it will be linked to fiber-optic, through which light will be propagated to the proposed PCF. When the incoming wave and the surface plasmon wave have the same frequency, the SPR phenomenon occurs in PCF, resulting in high light absorption and an SPR dip at the output. This resonance dip may shift depending on slight changes in analyte RI and can be measured by an optical spectrum analyzer.

As shown in **Figure 8.6**, the AS curve redshifts as the RI and associated resonant wavelengths increase. As the peak of clipping loss decreases, the amplitude sensitivity decreases, so we maintained observations up to RI 1.42 at the x-pole and 1.45 at the y-pole. The highest amplitude sensitivity achieved by the amplitude interrogation method is 4603 RIU^{-1} for x-polarization and 8485 RIU^{-1} for y-polarization, indicating that our design is highly functional and maintainable.
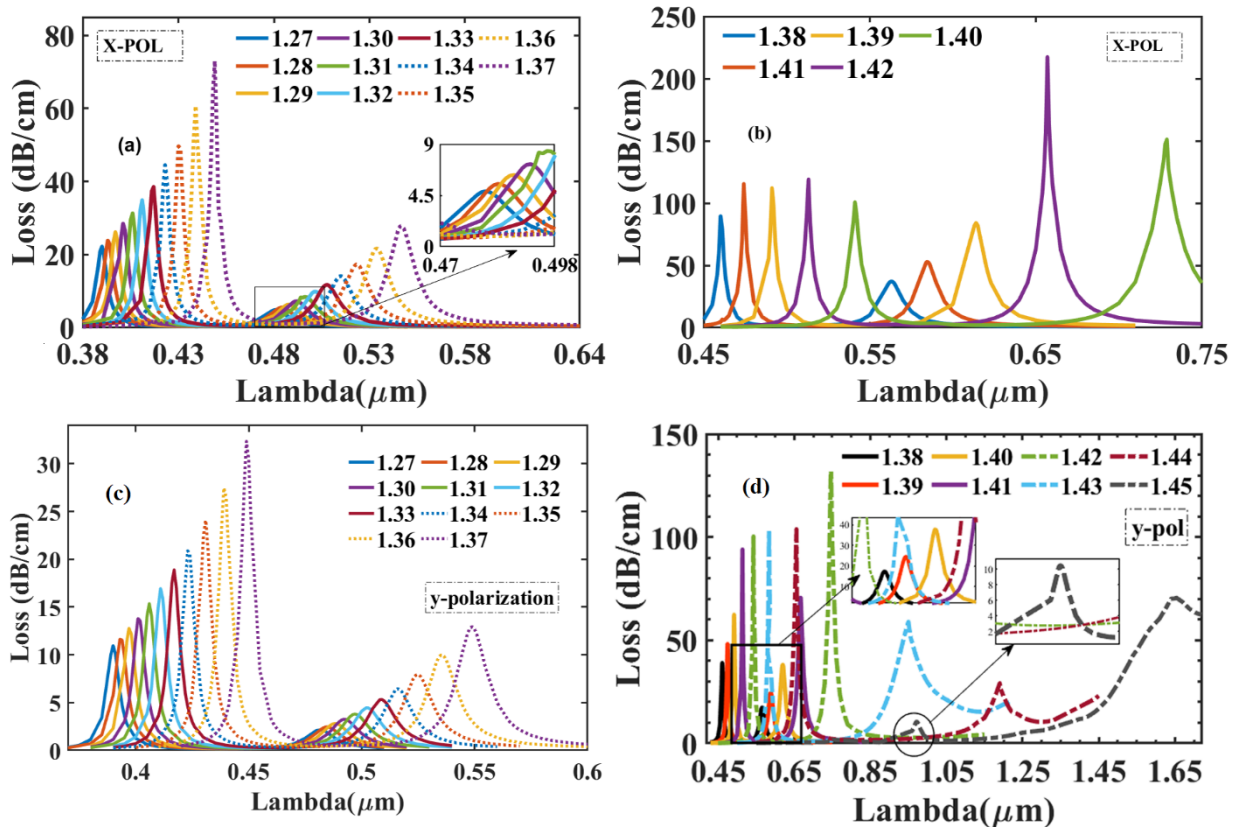
Figure 8.5: Confinement loss within RI span (a) 1.27-1.37 (b) 1.38-1.42 for x-pol (Structure A) within RI span (c) 1.27-1.37 (d) 1.38-1.45 and for y-pol (Structure B)

8.4.4 Maximum wavelength sensitivity

The relativistic efficiency of perception as a function of wavelength or frequency is known as spectral sensitivity. The maximum sensitivity of X polarization is 7200nm / RIU. This is because the resonance wavelength shifts from 657 nm to 729 nm when the RI variation using the equation shown in the wavelength survey method is 1.41 to 1.42.A maximum wavelength sensitivity of 46300 nm / RIU is observed with y-polarization (Structure B).
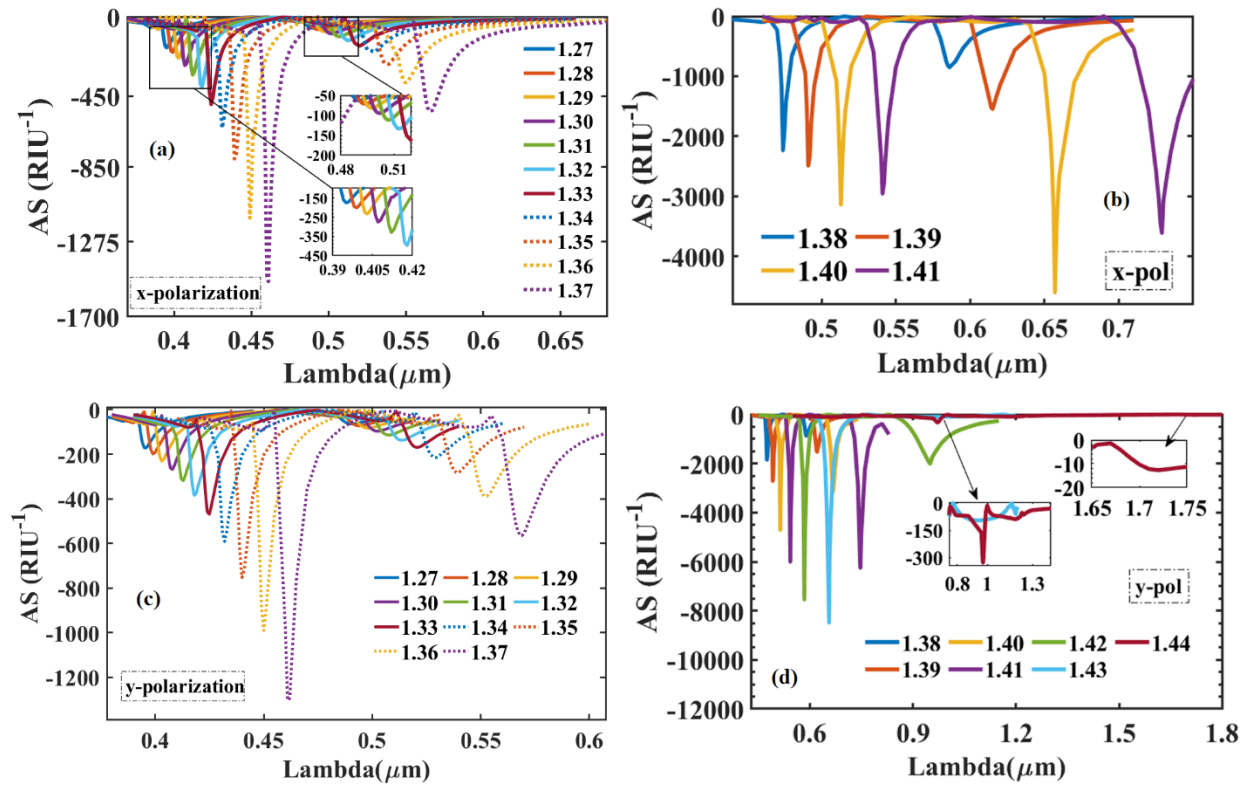
Figure 8.6: Amplitude sensitivity for x-pol (Structure A) within RI span (a) 1.27-1.37 (b) 1.38-1.41 and for y-pol (Structure B) within RI span (c) 1.27-1.37 (d) 1.38-1.44.

8.4.5 Higher linearity

A sensor with a higher linearity is required for effective calibration. We examined our sensor's performance using regression analysis methods while changing different parameters and monitoring sensing performance for various analyte RIs, as shown in fig.8.7. The linear fitting equation for x polarization in our initial model has a coefficient value of $R^2 = 0.90613$, which is closer to 1. High sensor linearity is a criterion for evaluating sensors, particularly for analytes with a higher RI. The quadratic fitting equation is shown in the same image with a coefficient value of 0.9908. As a result, 2nd order fitting is optimum for predicting sensor performance for structure

A. The polynomial equation can be fitted to 4th order guaranteeing high-quality sensor performance, for y polarization (structure B) with $R^2 = 0.99312$, as illustrated in fig. 8.7(b).

8.4.6 High figure of merit

A figure of merit (FOM) is a metric that measures how well a gadget performs in comparison to its peers. A high FOM number can be used to force the sensor to improve its quality of performance. A smaller FWHM (Full Width Half Maxima) value might result in a higher quantity of FOM, as shown by the equation
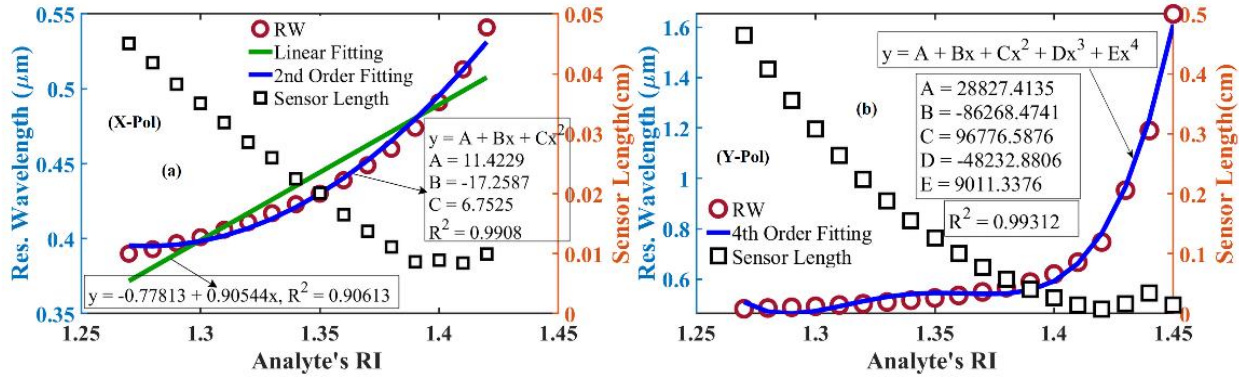
Figure 8.7: Polynomial fitting curve and sensor length for (a) x-pol 1st peak (Structure A) (b) y-pol (Structure B) 2nd peak

Our design has an extremely high FOM value of 2923 RIU^{-1} for y polarization and 1118 RIU^{-1} for x polarization when optimized. To the best of our knowledge, this substantially larger value of FOM has never been investigated while preserving a double peak, hence our sensor outperforms earlier studies[46], [47].The characteristics of two distinct resonance conditions are illustrated in table 1 and 2.

Table 8.1: Sensor characteristics within RI range (Structure A)

RI	1st Peak				2nd Peak			
(X-POL)	RW	CL	AS	WS	RW	CL	AS	WS
	(nm)	(dB/cm)	(RIU^{-1})	(nm/RIU)	(nm)	(dB/cm)	(RIU^{-1})	(nm/RIU)
1.27	390	22.20	174.46	300	481	4.86	63.08	300
1.28	393	23.87	200.88	400	484	5.51	71.26	300
1.29	397	26.14	233.48	400	487	6.24	81.57	500
1.30	401	28.48	275.34	500	492	7.25	94.78	400

1.31	406	31.31	329.25	500	496	8.41	111.75	600
1.32	411	34.93	397.38	600	502	9.86	133.61	600
1.33	417	38.54	496.80	600	508	11.72	164.82	700
1.34	423	44.52	630.37	700	515	14.13	199.65	800
1.35	430	49.66	804.89	900	523	17.28	273.2	1100
1.36	439	60.70	1140.5	1000	534	21.67	373.8	1300
1.37	449	72.99	1500	1100	547	27.82	536	1600
1.38	460	89.59	2234	1400	563	37.19	853.29	2200
1.39	474	115.5	2490.4	1700	585	52.74	1547	3500
1.40	491	112.2	3139	2200	620	84.17	4602.67	3700
1.41	513	119	2957	2800	657	217.4	3609.94	7200
1.42	541	100.8	---	---	729	151.2	---	---

8.4.7 10^{-6} order of resolution

Resolution is another important parameter for sensors, since it influences how well the system can detect and portray tiny fluctuations in RI quantification. When the RI is held at 1.40, the amplitude interrogation approach offers a maximum resolution of 2.1710^{-6} RIU for x polarization and 1.1810^{-6} RIU for y polarization.

Table 8.2: Sensor characteristics within RI range (Structure B)

RI	1st Peak				2nd Peak			
(Y-POL)	RW (nm)	CL (dB/cm)	AS (RIU^{-1})	WS (nm/RIU)	RW (nm)	CL (dB/cm)	AS (RIU^{-1})	WS (nm/RIU)
1.27	390	10.97	171.70	300	482	2.15	63.87	300
1.28	393	11.62	199.23	400	485	2.46	72.53	300
1.29	397	12.78	230.59	400	488	2.81	83.17	400
1.30	401	13.80	268.40	500	492	3.25	96.47	500
1.31	406	15.37	318.59	500	497	3.79	114.07	500

1.32	411	16.94	385.16	600	502	4.46	137.40	700
1.33	417	18.90	469.17	600	509	5.32	169.52	700
1.34	423	20.89	591.54	800	516	6.45	215.33	900
1.35	431	24.09	753.59	800	525	7.94	282.53	1000
1.36	439	27.47	990.42	1000	535	9.96	388.85	1400
1.37	449	32.35	1301.9	1200	549	12.94	564.88	1700
1.38	461	39.00	1852.2	1400	566	17.39	876.62	2200
1.39	475	48.18	2714.9	1700	588	24.56	1522.7	3200
1.40	492	62.37	4706.4	2200	620	38.05	3166.9	4700
1.41	514	94.03	6006.3	2900	667	70.61	6252.1	8000
1.42	543	100.4	7545.2	4100	747	132	2078.8	20600
1.43	584	103.8	8485.2	7200	953	60.63	62.37	23700
1.44	656	103.9	327.26	31600	1190	29.20	12.69	46300
1.45	972	10.43	---	---	1653	70.51	---	---

Another approach to determining sensor resolution is to use a wavelength interrogation method that can be calculated using the equation given below where indicates the minimum wavelength resolution of 0.1 nm. The maximum wavelength resolution is 1.38×10^{-5} RIU and 2.16×10^{-6} RIU for x-pol and y-pol, respectively. As a result, the virtual sensor can accurately detect RI fluctuations on a 10^{-6} scale.

8.4.8 Novel double peak shift sensitivity and RI detection

It has been previously discussed that the proposed structure of this sensor produces two distinct loss peaks at two different resonant wavelengths for a given index of refraction. Here, Figures 8.8 (a) and 8.8 (b) show the relationship between the 1 and 2 loss peaks and the corresponding Analyte RIs of both structures. From these figures, the resonant wavelength interval increases the index of refraction of the analyte from 1.32 to 1.45 for structure B and from 1.33 to 1.41 for structure A. This is due to a continuous double peak shift. An extension of this notion of the relationship between peak-to-peak distances and the RI of the object to be analyzed has introduced a new sensitivity parameter called double peak shift sensitivity. This sensor has achieved double peak

shift sensitivity of 4400 RIU/nm and 16500 RIU/nm for x-polarization mode and y-polarization mode respectively.

Next, from Figures 8.9 (a) and 8.9 (b), we can see that the loss intensities of the primary and secondary peaks are not equal. This occurs because the index of refraction remains the same, but the maximum amount of energy transferred from core mode to spp mode at different resonance wavelengths varies as the light frequency changes due to light scattering. Furthermore, if the RI of the analysis object is different from 1.27 to 1.39 for structure A and 1.27 to 1.4 for structure B, the difference in loss intensity between the primary peak and the secondary peak will also be larger. This property can be used to separate one analyte from another based on index of refraction. The relationship between the difference in loss peak intensity and the index of refraction can also be expressed by the following fourth-order polynomial function.
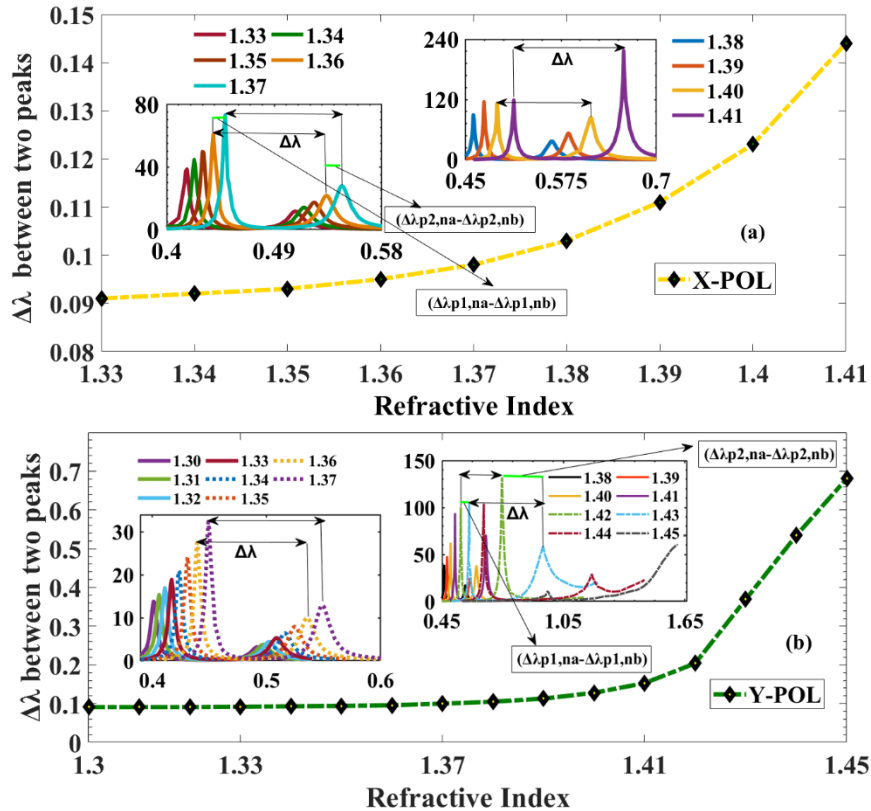
Figure 8.8: Separation of resonance wavelengths of two peaks Vs RI for (a) structure A (b) structure B

$$\Delta_{loss_x} = 378257.2908 \pm 1190993.9355 \times n_a + 1406026.9126 \times n_a^2 \pm 737656.1412 \times n_a^3$$
$$+145128.3869 \times n_a^4, R^2 = 0.99891 \qquad (8.1)$$

$$\Delta_{loss_y} = -344206.164 + 1036629.4673 \times n_a \pm 1169856.8143 \times n_a{}^2 + 586273.3377 \times n_a{}^3$$
$$\pm 110075.2671 \times n_a{}^4, R^2 = 0.99788 \qquad (8.2)$$

Here Δ_{loss_x} and Δ_{loss_y} represent double peak loss intensity difference between first and secondary peaks respectively for x-polarization (structure A) and y-polarization (structure B) and n_a is the refractive index of an unknown analyte. The result from double peak analysis are illustrated in the given table 8.3.

Figure 8.9: Difference of two loss peak magnitudes vs RI for (a) structure A (b) structure B

Table 8.3: Results from Double peak shift analysis

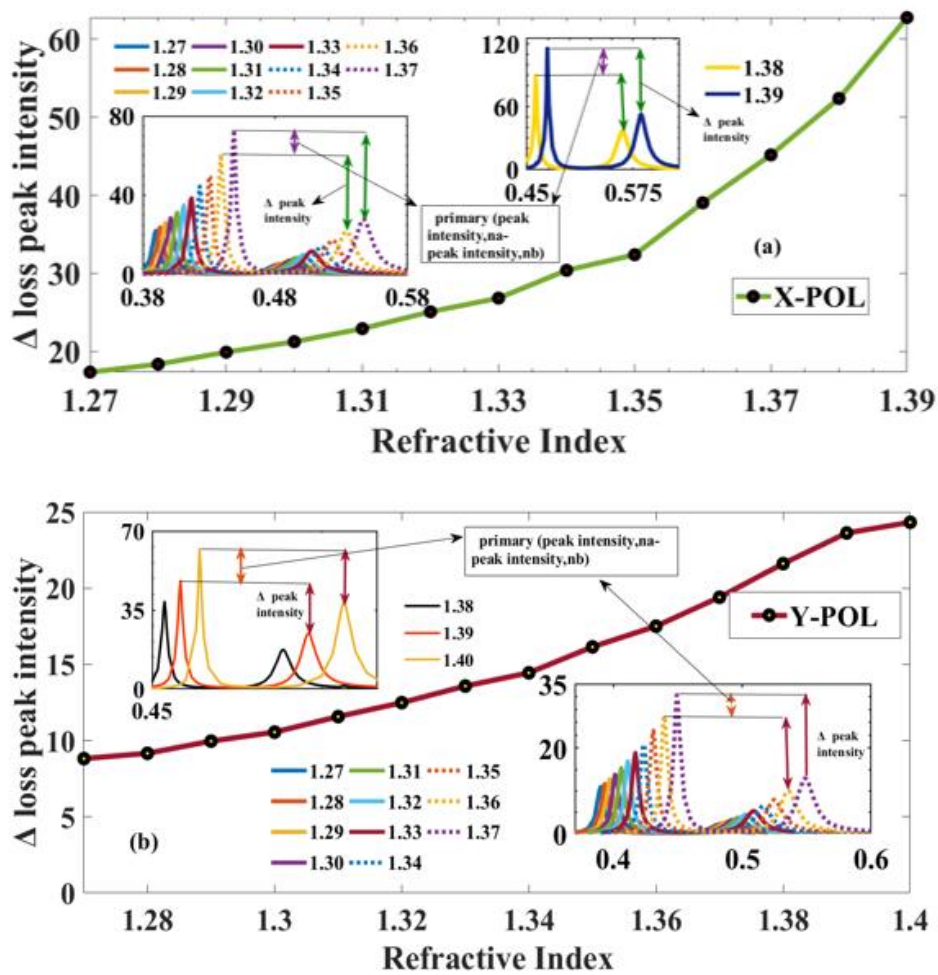| Analyte RI	$\Delta\lambda_{p1-p2}$,X-POL	$\Delta\lambda_{p1-p2}$,Y-POL	Double peak shift sensitivity(nm/RIU)		Analyte RI	Δ_{loss_x}	Δ_{loss_y}
			X-POL	Y-POL	1.27	17.33561	8.8172
1.32	-	0.091	-	100	1.28	18.35309	9.16547
1.33	0.091	.092	100	100	1.29	19.89394	9.96379
1.34	0.092	.093	100	100	1.30	21.23338	10.55541
1.35	0.093	.094	200	200	1.31	22.90808	11.57384
1.36	0.095	.096	300	400	1.32	25.06979	12.48796
1.37	0.098	0.1	500	500	1.33	26.8195	13.58011
1.38	0.103	.105	800	800	1.34	30.3854	14.44647
1.39	0.111	.113	1800	1500	1.35	32.3779	16.14888
1.40	0.123	.128	1500	2500	1.36	39.0334	17.50627
1.41	0.144	.153	4400	5100	1.37	45.167	19.4078
1.42	-	.204	-	16500	1.38	52.40222	21.61073
1.43	-	.369	-	16500	1.39	62.76319	23.62331
1.44	-	.534	-	14700	1.40	-	24.326
1.45	-	.681	-	-	1.41	-	-

8.5 Fabrication Possibilities

One of the most important elements of LSPR-based plasmonic sensors is the manufacturing outlook. The proposed sensor uses circular air holes, which simplifies the practical implementation of the sensor. Figure 8.10 shows the estimated manufacturing process for the proposed sensor. Stack-and-pull manufacturing techniques can be used to assemble the core and clad parts of the sensors provided [48]. First, two different types of capillaries (thick-walled capillaries and thin-walled capillaries) are created. The size of the capillaries will be 100 times the suggested size. These capillaries are placed with fixing rods according to the proposed sensor air hole configuration. Then an intermediate preform called a wand is drawn until the proposed dimensions are reached. A two-step photolithography process can be performed to achieve the AZO layer and the gold layer. First, one of the plasmonic layers is deposited around the fiber surface using CVD (Chemical Vapor Deposition) technology [49]. Then using mask over the targeted area plasmonic layer 1 will be done. The same process will be adopted to carry out plasmonic layer 2.

Furthermore, a sensing layer will be built with two pumps, one of which will allow analytes to enter the layer and the other will be used to evacuate the sensing layer [50]. Following these procedures will allow the suggested sensor to be manufactured using conventional manufacturing methods.
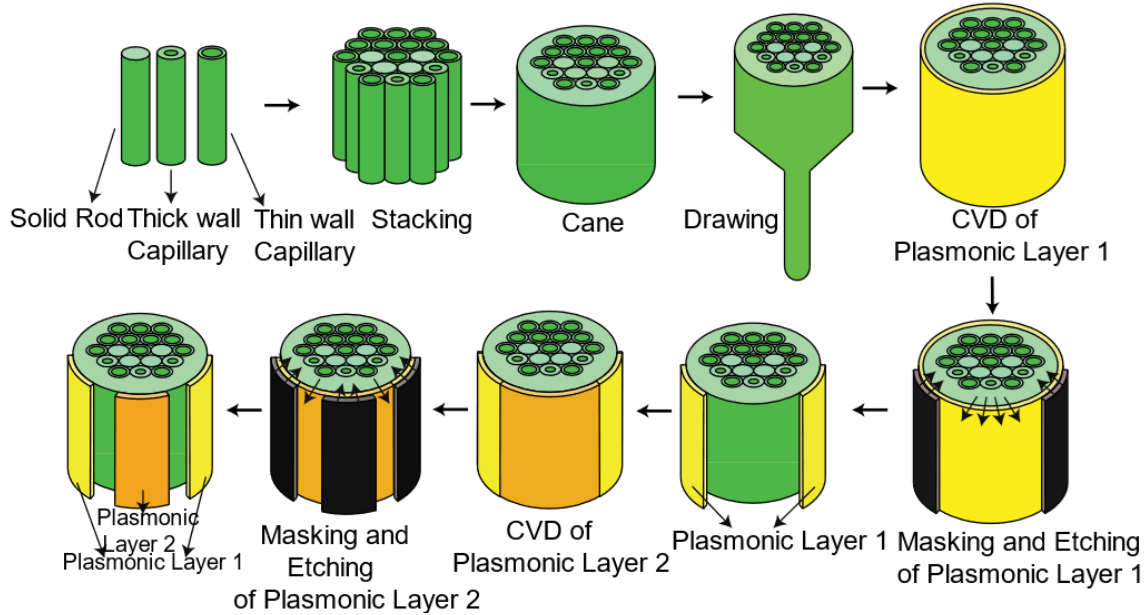
Fig. 8.10: Fabrication of the proffered sensor

8.6 Comparative study:

The proffered structures are compared with previous works in the given table.

Table 8. 4: The proffered sensor comparing with other previously recorded works

Ref	RI Range	AS$_{max}$ (RIU^{-1})	WS$_{max}$ (nm/RIU)	FOM (RIU^{-1})	Double peak sensitivity (RIU/nm)
[32]	1.32-1.41	1170	34000	310	---
[46]	1.33-1.45	---	7900	93.7	---
[20]	1.32-1.43	5060	41500	1053.7	---
[51]	1.32-1.34	---	5000	167	---
[47]	1.33-1.40	---	11600	---	---
[52]	1.35-1.38	---	18900	---	---
[53]	1.33-1.45	5503	75000	904	---

| This work | Structure A | 1.27-1.42 | 4602.67 | 7200 | 1118 | 4400 |
| | Structure B | 1.27-1.45 | 8485.2 | 46300 | 2923 | 16500 |

8.7 Conclusion:

The proposed new structure of the sensor enables operation in the visible and NIR regions, opening the sensor to broadband applications and providing biomedical sensing for deep tissue penetration. This sensor shows a maximum amplitude sensitivity of 8485.2 RIU^{-1} and maximum wavelength sensitivity of 46300 RIU / nm for structure B y-polarization, and maximum wavelength sensitivity of 7200 RIU / nm and an amplitude sensitivity of 4602.67 RIU^{-1} for x-polarization. Structure A. In addition, the maximum amplitude resolution is 1.18×10^{-6} RIU and the maximum wavelength resolution is 2.16×10^{-6} RIU, and the figure of merit of y-polarization is as high as 2923.2. Overall, using AZO as an intermediate plasmonic material could be a better option for high sensing properties. Numerical studies are performed separately for both loss peaks, then double peak shifts are considered as a whole. This contributes to the phrase "double peak shift sensitivity," which is a new sensitivity term. A maximum D.P. sensitivity of 16500 is also achieved with the sensor. To summarize, the proposed sensor has raised the likelihood of reliable detection of a wide range of analytes while also widening the scope of distinct sensing parameter techniques..

Chapter 9

Proposed Design 04: D-shaped PCF-based polarization filter for single tuning with gold coating for S+U band applications

9.1 Introduction

This chapter analyzed a gold-coated photonic crystal fiber-based single polarizing filter with a D-shape in the wavelength range of 1.408 μm to 1.652 μm for specific applications in the S + U band. An asymmetrical arrangement of air holes is adopted to allow for high birefringence and crosstalk. This filter exhibits strong filter characteristics with a large confinement loss of 1682.5 dB / cm in the x-direction at a wavelength of 1.652 μm, while exhibiting very low intensity with y-polarization of only 85.89 dB / cm. In addition, its crosstalk can reach up to 1387 dB, with a 160 dB extinction ratio at a higher wavelength of 1.652 μm for a 1000 μm fiber length. Therefore, this filter can be used for both the optical S-band and U-band of the electromagnetic spectrum.

9.2 Geometrical Structure:

A cross-section of the X polarizing filter is shown in Figure 9.1 below. This two-dimensional structure was constructed using the perfect vector finite element method (FEM) using the Comsol Multiphysics 5.3a software. The exterior of the fiber is composed of a perfectly matched layer (PML), which is used to effectively reduce outward radiation, allowing for more detailed computational studies. Three different sizes, namely d_1, d_2, and d_3 air holes, are located in several layers of the clad region of the hexagonal lattice and greatly affect the performance of the polarizing filter. The base material employed here is fused silica. An asymmetrical structure was adopted to help create a polarizing effect. Most of the ventilation holes distributed over the entire shell have a diameter of $d_1 = 0.45$ with an even spacing between them of $\Lambda = 1$. Some layers are interrupted by inserting air holes twice their size in polarization mode. These stomata, with diameter $d_2 = 0.9$, suppress the regularity of the structure to improve the birefringence of the fiber, thereby contributing to the polarizing effect. The innermost layer consists of a combination of these two types of stomata that affect the shape of the hollow core and fix the light inside the core. A large stoma of 1.05 in diameter with a gold film coating thickness, $tg = 20$ nm, amplifies the coupling between the core and SPP modes. Gold was chosen as a plasmonic material.
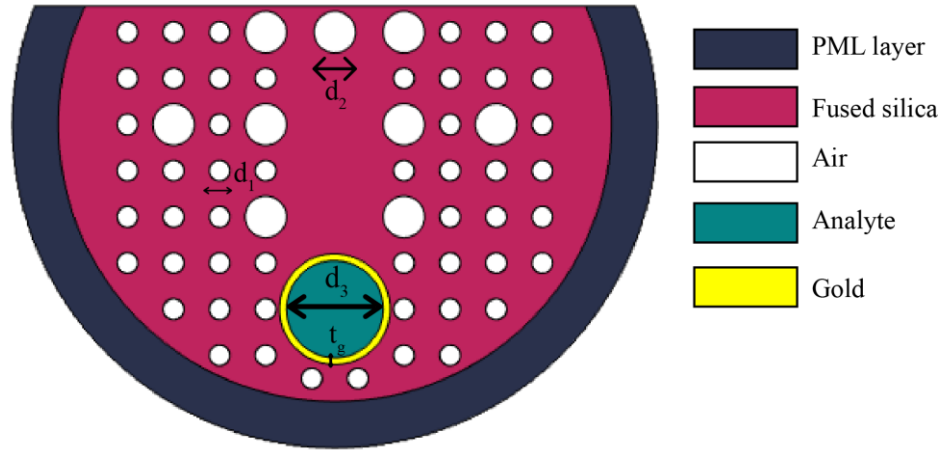
Fig 9.1: 2-dimensional view of the presented single-polarization filter

9.3 Distribution of electric field:

The distribution of electric fields for the core modes of the two polarizers, as shown in Figure 9.2. (a & b), represents the energy trapped in the fiber core. In Figure 9.2(c), the optical energy distributions of the related SPP modes can also be detected near the gold mantle. Under phase matching condition, complete coupling between these two modes occurs, leading to large loss of limit. The dispersion characteristics of the filter have been described in Fig. 9.3. The blue and red graphs demonstrate that at resonant wavelength 1.408 μm, a strong coupling occurs between the polarized x-mode and the SPP mode, where the effective indices of the two modes become the same.
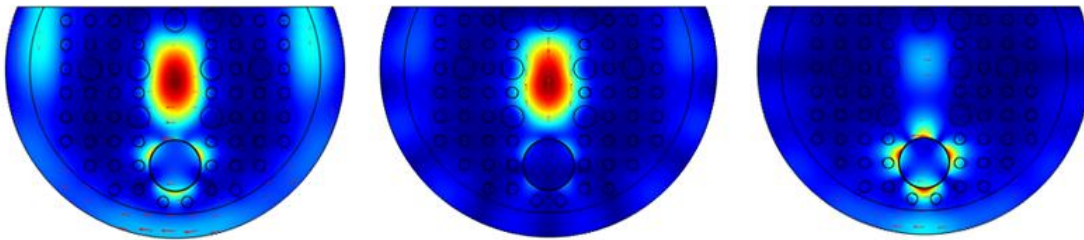
Fig. 9.2. Illustration of the electric field distribution of the (a) x-polarization mode, (b) y-polarization mode, and the (c) SPP mode
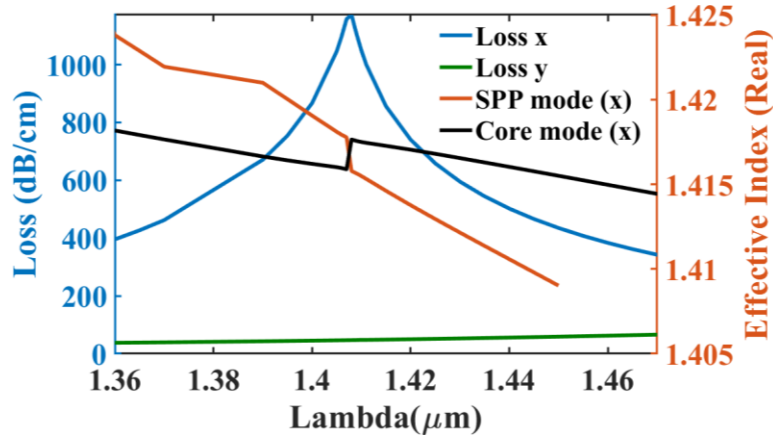
Fig. 9.3. Loss spectra of the x and y-pol and the SPP mode with respect to wavelength

9.4 Behavior of the proposed filter:

9.4.1 Effect of structural parameters on confinement loss:
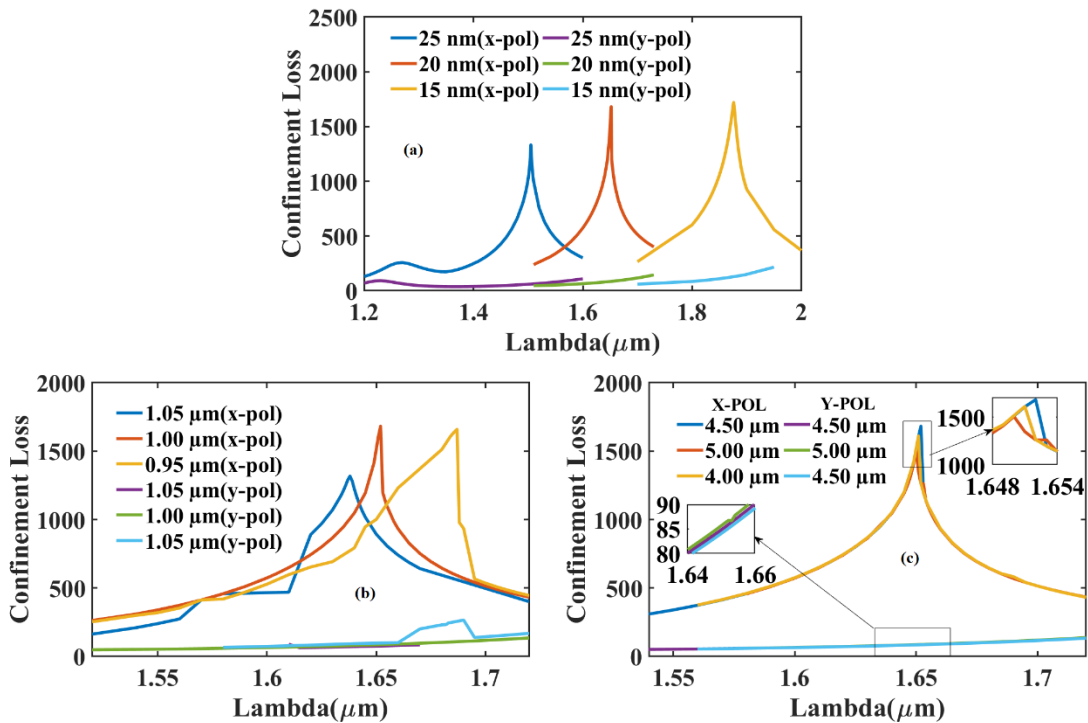
Fig. 9.4 Loss spectra for variation of (a) thickness of gold layers (t_g) (b) diameters of large air holes (d_3) (c) diameters of holes (d_1) for asymmetrical purposes

From Figure 9.4. (a), it can be observed that the loss increases until the highest value at the resonant wavelength and then decreases as the wavelength increases. The maximum limit loss for 15 nm,

20 nm and 25 nm is 1720,915 dB/cm, 1682,499 dB/cm and 1333.437 dB/cm, respectively. For 25 nm, 20 nm, and 15 nm at the respective resonant wavelengths, the loss for y-polarization is 61.24806 dB/cm, 85.89413 dB/cm, and 128.6742 dB/cm. Therefore, the loss spectra of the x- and y-direction modes are orthogonal around the resonant wavelength region. Furthermore, if the thickness of the gold is reduced at both polarizations, the loss of the limit will increase with the extension of the resonance wavelength. The peak values of loss for different diameters of large air holes are1317.506 dB/cm, 1682.499 dB/cm, and 1658.973 dB/cm respectively for 1.05 μm, 1 μm, and 0.95 μm in case of x-polarization. From Fig. 9.4. (b), a conclusion can be drawn that confinement loss escalates with lowering the diameter of these air holes. There is no significant effect of changing the stomatal diameter on the confinement loss for y polarization compared with x polarization. From Fig. 9.4. (c), it can be noticed that the loss peak develops from 0.4 μm to 4.5 μm and then decreases for 0.5 μm as diameter of the air holes purposed for asymmetry. The highest loss at 1.652 μm is calculated as 1682.499 dB/cm.

9.4.2 Confinement loss ratio:

From the figure 9.5, ,it can be seen that CLR increases first and then decreases with the increment of the wavelength for analyte RI 1.41. The confinement loss of x polarization was calculated to be 19.58 times the confinement loss of y-pol at the peak of CLR.
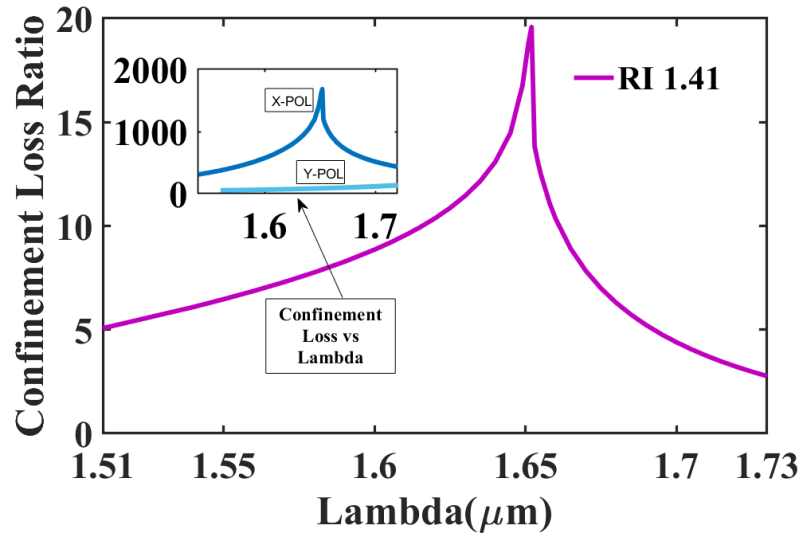
Fig 9.5 : CLR as a function of wavelength

9.4.3 Effect of structural parameters on Crosstalk:

From figure 9.6, it can be seen that fiber length along with the diameter of air holes significantly affects the values of crosstalk. The 20 nm gold as plasmonic layer with a length of 1000 μm has the highest crosstalk of 1387 dB, which is considered as the optimal value for further investigation. From the given graphs,it can be concluded that diameter of 1000 nm for large air holes and 450 nm for air holes of symmetry purposes give the best possible result during cross talk analysis.
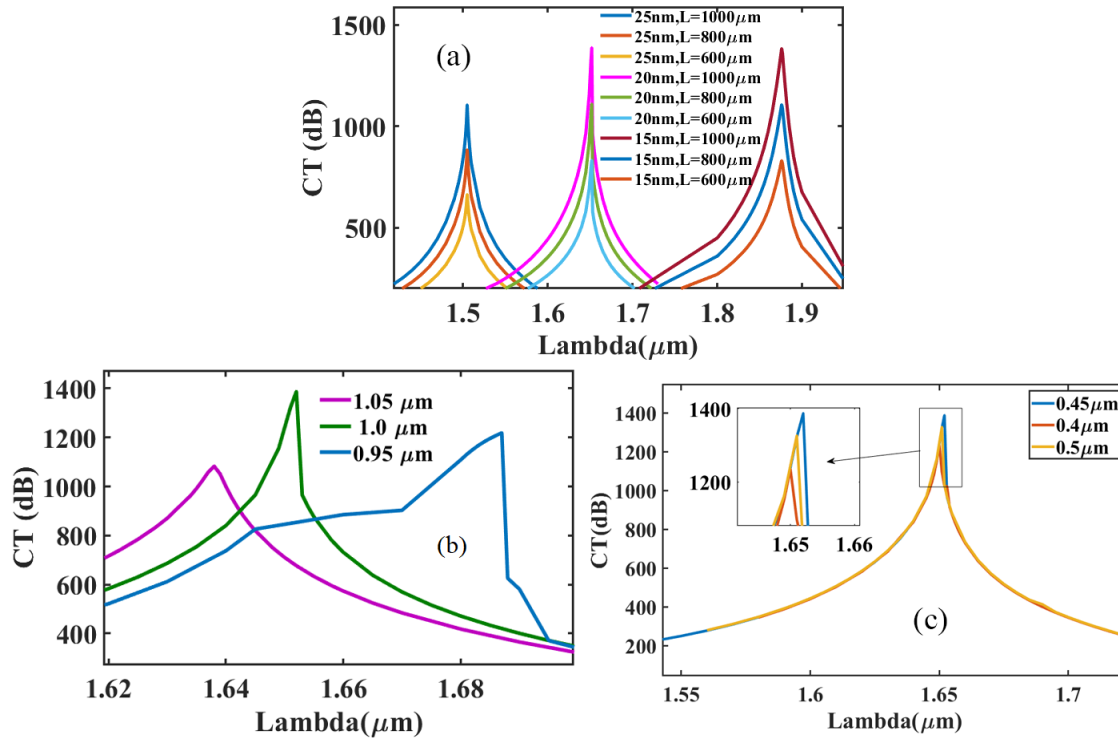
Fig 9.6: Cross-talk as a function of wavelength for (a) thickness of gold layers (t_g), (b) diameters of large air holes (d_3) and (c) diameters of asymmetrical holes (d_1)

9.4.4 Effect of structural parameters on output power:

Figures 9.7 and 9.8 show the output power characteristic as a function of wavelength change. The output power of x-polarization drops as the wavelength value increases, while structural characteristics have no significant effect on the output power. As seen in Fig. 9.8, output power for y-polarization decreases more with each wavelength increment than for x-polarization. The output power of x-polarization is closer to 0.

Fig. 9.7. Output power for variation of (a) gold thickness, (b) diameter of large air hole and (c) diameter of (asymmetry) air hole for x-polarization as a function of wavelength

9.4.5 Effect of structural parameters on extinction ratio:

From figure 9.9, it can be seen that the extinction ratio at first rises and then falls for every structural parameter plasmonic material, with the rise of wavelength. After the crucial analysis, it was found that 20 nm layer of diameter of 1000nm large air holes, and 450 nm of other air holes for symmetry purposes give the best value of extinction ratio.

9.5 Comparison Analysis

Table 9.1: Analogy between the suggested design and some prior works

Reference	Resonance wavelength(nm)	Length (mm)	Cross-talk (dB)	Extinction Ratio (dB)
[54]	1550	0.035	-22.2	-
[55]	1520	0.023	-46.4	-
[56]	1550	1	249.5	-
[57]	1570	1	447.5	60
[4]	1310	2	-	-478
[58]	1550	1	-30	-
[24]	1540	1	-853	-
[59]	1550	1	326.7	-
This Work	1652	1	1387	160

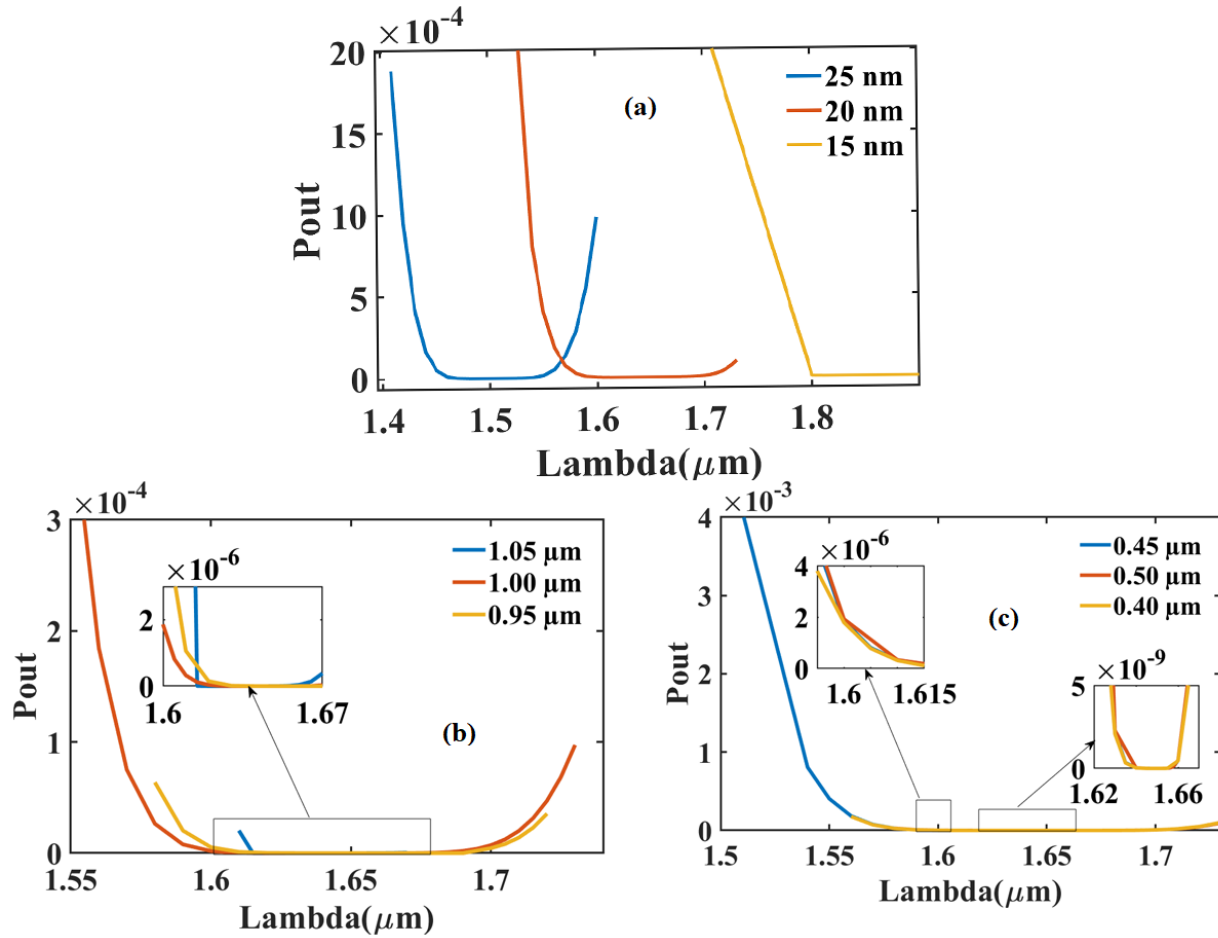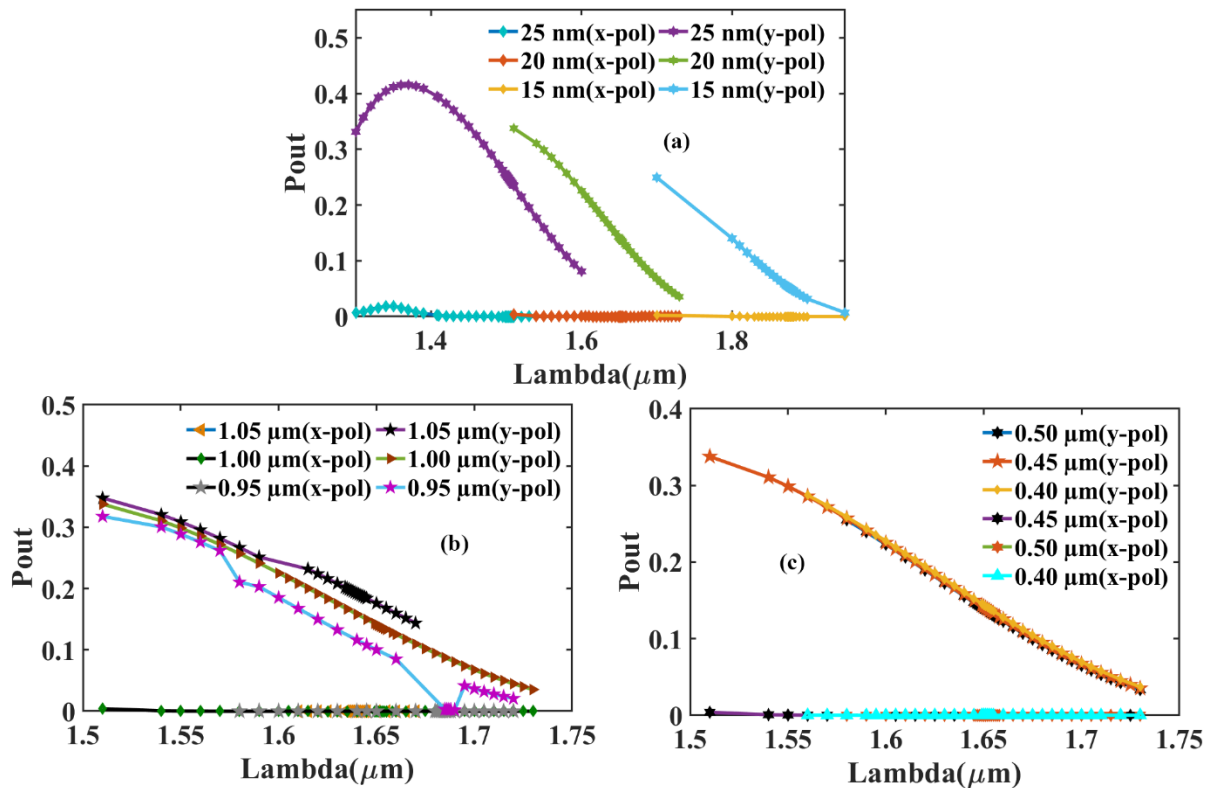**Fig: 9.8 Variation of output power for variation of (a) gold thickness, (b) diameter of large air hole and, (c) diameter of other air holes as a function of wavelength**
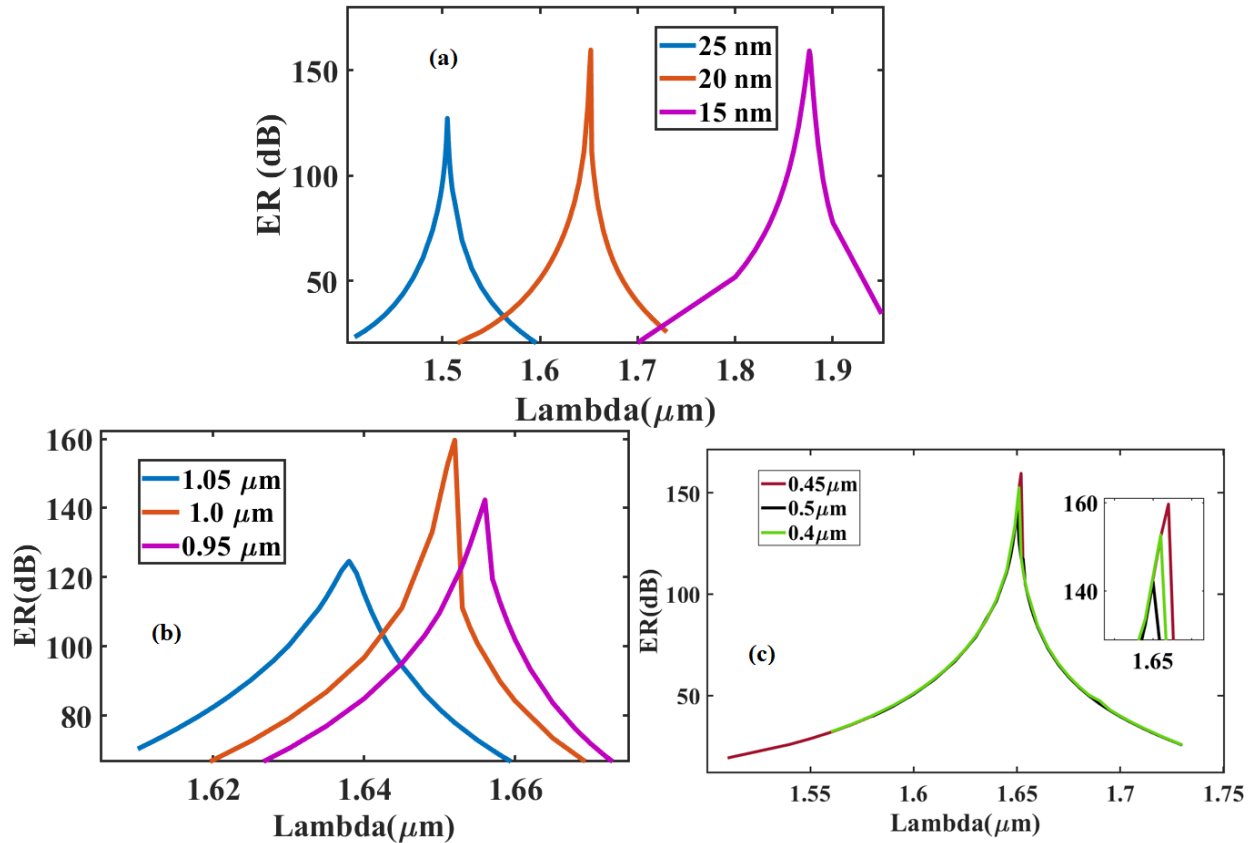
Fig. 9.9. Extinction ratio investigation for (a) different thickness of gold layers (t_g), (b) different diameters of large air holes (d_3) and (c) different diameters of asymmetrical holes (d_1)

9.6 Conclusion:

The proffered filter operates within a wavelength span of 1408nm to 1652nm which is not similar to a typical communication window. This feature makes this single polarization filter different from others. The fiber length the diameter of large air holes, plasmonic layer thickness, and other air holes were investigated to get the best filtering performance. For a specific resonant wavelength of 1652 nm, a lower CL value of 85,8941 dB/cm can be obtained. for y polarization whereas the maximum value for CL in x-polarization mode obtained is 1682,499 dB/cm. Other filtering characteristics have also been analyzed. So, it can be understood that the proffered filter showcases great potential for S to U band applications.

Chapter 10

Conclusion and Future Prospect

10.1 Conclusion:

We started our work with PCF based RI sensor which detected milk sensitivity, then moved our motivation towards SPR based RI sensors due to its advantages like label-free detection and flexible nature. During the second work of ours, we discovered the multi-purpose SPR sensors which contribute to the research of temperature and magnetic field strength sensors. Moreover, SPR technique proved to be a strong candidate for ultra-high sensitivity and fabrication friendliness. As we dived deep into the research of photonic crystal fibers, we got introduced to the concept of LSPR based refractive index sensors which contribute a lot to the study of nano biosensors. In all of these, we investigated almost similar parameters like amplitude sensitivity, wavelength sensitivity, figure of merit, confinement loss, etc. But as we moved forward towards another implementation of SPR technique as single polarization filter, new performance parameters like cross talk, extinction ratio, etc. Additionally, we utilized the finite element method in COMSOL Multiphysics to build our designs and investigate the performances of sensors and filters. In a nutshell, this whole work was based on different applications and implementations of photonic crystal fibers which contribute to the study of different analyte detection and broadband application.

10.2 Future prospects:

In our designs, we have mostly used circular air holes of different diameters along with different placements of air holes. Adding to that we also used fused silica as background material mostly in designing our fibers. We believe that there are many opportunities to make further advancements for different applications of photonic crystal fiber along with improvements in the performance of fibers such as-

1. Air holes of different shapes like elliptical and rectangular can be used to further investigate the performance of any PCF based sensor or filter.

2. The operating wavelength range of PCFs can be expanded and a certain focus can be given for dual-polarization filters.

3. Different plasmonic materials such as graphene, TiN, etc separately or simultaneously with AZO or gold can be used to get better sensing performances.

4. Multi-channel-based refractive index sensor for simultaneous detection of multiple analytes can be implemented.

5. Work on metal grating-based sensors for specific applications can also be carried out.

References

[1]   D. R. Thvenot, K. Toth, R. A. Durst, and G. S. Wilson, "Electrochemical biosensors: Recommended definitions and classification (Technical Report)," *Pure Appl. Chem.*, vol. 71, no. 12, pp. 2333–2348, 1999, doi: 10.1351/pac199971122333.

[2]   M. R. Islam *et al.*, "Surface plasmon resonance based highly sensitive gold coated PCF biosensor," *Appl. Phys. A Mater. Sci. Process.*, vol. 127, no. 2, 2021, doi: 10.1007/s00339-020-04162-5.

[3]   V. Kaur and S. Singh, "A dual-channel surface plasmon resonance biosensor based on a photonic crystal fiber for multianalyte sensing," *J. Comput. Electron.*, vol. 18, no. 1, pp. 319–328, 2019, doi: 10.1007/s10825-019-01305-7.

[4]   N. Chen, X. Zhang, M. Chang, X. Lu, and J. Zhou, "Broadband Plasmonic Polarization Filter Based on Photonic Crystal Fiber with Dual-Ring Gold Layer," *Micromachines*, vol. 11, no. 5, May 2020, doi: 10.3390/MI11050470.

[5]   M. R. Islam *et al.*, "Highly birefringent gold-coated SPR sensor with extremely enhanced amplitude and wavelength sensitivity," *Eur. Phys. J. Plus*, vol. 136, no. 2, pp. 1–14, Feb. 2021, doi: 10.1140/epjp/s13360-021-01220-6.

[6]   H. F. Fakhruldeen and A. Z. Ghazi Zahid, "An Overview of Photonic Crystal Fiber (PCF)," no. April 2019, 2019, [Online]. Available: www.tnsroindia.org.in.

[7]   J. Qin, Z. Meng, J. Gao, Z. Fan, and X. Wang, "Surface plasmon enhanced polarization filter of high birefringence photonic crystal fiber with a partial core based on filled silver nanowire," *Opt. Fiber Technol.*, vol. 60, no. August, p. 102342, 2020, doi: 10.1016/j.yofte.2020.102342.

[8]   M. A. Islam, M. R. Islam, S. Siraz, M. Rahman, M. S. Anzum, and F. Noor, "Wheel structured Zeonex-based photonic crystal fiber sensor in THz regime for sensing milk," *Appl. Phys. A Mater. Sci. Process.*, vol. 127, no. 5, pp. 1–13, 2021, doi: 10.1007/s00339-021-04472-2.

[9]   X. Yang, Y. Lu, B. Liu, and J. Yao, "Design of a Tunable Single-Polarization Photonic Crystal Fiber Filter with Silver-Coated and Liquid-Filled Air Holes," *IEEE Photonics J.*, vol. 9, no. 4, 2017, doi: 10.1109/JPHOT.2017.2720590.

[10]   Y. Gamal, B. M. Younis, S. F. Hegazy, Y. Badr, M. F. O. Hameed, and S. S. A. Obayya, "Highly efficient modified dual D-shaped PCF polarization filter," *Opt. Fiber Technol.*, vol. 62, no. January, p. 102459, 2021, doi: 10.1016/j.yofte.2021.102459.

[11]   M. R. Islam *et al.*, "Design and numerical analysis of a gold-coated photonic crystal fiber

based refractive index sensor," *Opt. Quantum Electron.*, vol. 53, no. 2, Feb. 2021, doi: 10.1007/s11082-021-02748-8.

[12]   S. Islam *et al.*, "Extremely low-loss, dispersion flattened porous-core photonic crystal fiber for terahertz regime," *Opt. Eng.*, 2016, doi: 10.1117/1.oe.55.7.076117.

[13]   M. R. Hasan, S. Akter, T. Khatun, A. A. Rifat, and M. S. Anower, "Dual-hole unit-based kagome lattice microstructure fiber for low-loss and highly birefringent terahertz guidance," *Opt. Eng.*, 2017, doi: 10.1117/1.oe.56.4.043108.

[14]   M. R. Islam, M. A. Hossain, K. M. A. Talha, and R. K. Munia, "A novel hollow core photonic sensor for liquid analyte detection in the terahertz spectrum: design and analysis," *Opt. Quantum Electron.*, 2020, doi: 10.1007/s11082-020-02532-0.

[15]   K. Ahmed *et al.*, "Refractive Index-Based Blood Components Sensing in Terahertz Spectrum," *IEEE Sens. J.*, 2019, doi: 10.1109/JSEN.2019.2895166.

[16]   I. K. Yakasai, P. E. Abas, S. Ali, and F. Begum, "Modelling and simulation of a porous core photonic crystal fibre for terahertz wave propagation," *Opt. Quantum Electron.*, vol. 51, no. 4, pp. 1–16, Apr. 2019, doi: 10.1007/s11082-019-1832-x.

[17]   M. S. Islam *et al.*, "A Hi-Bi Ultra-Sensitive Surface Plasmon Resonance Fiber Sensor," *IEEE Access*, vol. 7, pp. 79085–79094, 2019, doi: 10.1109/ACCESS.2019.2922663.

[18]   S. Chakma, M. A. Khalek, B. K. Paul, K. Ahmed, M. R. Hasan, and A. N. Bahar, "Gold-coated photonic crystal fiber biosensor based on surface plasmon resonance: Design and analysis," *Sens. Bio-Sensing Res.*, vol. 18, pp. 7–12, Apr. 2018, doi: 10.1016/J.SBSR.2018.02.003.

[19]   M. R. M. Islam *et al.*, "Design and analysis of birefringent SPR based PCF biosensor with ultra-high sensitivity and low loss," *Optik (Stuttg).*, vol. 221, p. 165311, Nov. 2020, doi: 10.1016/j.ijleo.2020.165311.

[20]   M. Rakibul Islam, M. M. I. Khan, F. Mehjabin, J. Alam Chowdhury, and M. Islam, "Design of a fabrication friendly & highly sensitive surface plasmon resonance-based photonic crystal fiber biosensor," *Results Phys.*, vol. 19, p. 103501, Dec. 2020, doi: 10.1016/j.rinp.2020.103501.

[21]   H. Wang, X. Yan, S. Li, and X. Zhang, "Tunable surface plasmon resonance polarization beam splitter based on dual-core photonic crystal fiber with magnetic fluid," *Opt. Quantum Electron.*, vol. 49, no. 11, pp. 1–10, 2017, doi: 10.1007/s11082-017-1190-5.

[22]   H. Huang *et al.*, "A highly magnetic field sensitive photonic crystal fiber based on surface plasmon resonance," *Sensors (Switzerland)*, vol. 20, no. 18, pp. 1–15, 2020, doi: 10.3390/s20185193.

[23] M. Rakibul Islam, A. N. M. Iftekher, M. S. Anzum, M. Rahman, and S. Siraz, "LSPR Based Double Peak Double Plasmonic Layered Bent Core PCF-SPR Sensor for Ultra-Broadband Dual Peak Sensing," *IEEE Sens. J.*, vol. 22, no. 6, pp. 5628–5635, Mar. 2022, doi: 10.1109/JSEN.2022.3149715.

[24] C. Liu *et al.*, "The single-polarization filter composed of gold-coated photonic crystal fiber," *Phys. Lett. A*, vol. 383, no. 25, pp. 3200–3206, Sep. 2019, doi: 10.1016/J.PHYSLETA.2019.07.012.

[25] Q. Liu *et al.*, "Broadband Single-Polarization Photonic Crystal Fiber Based on Surface Plasmon Resonance for Polarization Filter," *Plasmonics*, vol. 10, no. 4, pp. 931–939, Aug. 2015, doi: 10.1007/S11468-015-9882-9.

[26] M. S. Islam *et al.*, "Experimental Study on Glass and Polymers: Determining the Optimal Material for Potential Use in Terahertz Technology," *IEEE Access*, 2020, doi: 10.1109/ACCESS.2020.2996278.

[27] "Silica fibers, explained by RP Photonics Encyclopedia; optical fiber, glass, fiber optics." .

[28] P. R. West, S. Ishii, G. V. Naik, N. K. Emani, V. M. Shalaev, and A. Boltasseva, "Searching for better plasmonic materials," *Laser Photon. Rev.*, vol. 4, no. 6, pp. 795–808, Nov. 2010, doi: 10.1002/LPOR.200900055.

[29] G. V. Naik, V. M. Shalaev, and A. Boltasseva, "Alternative Plasmonic Materials: Beyond Gold and Silver," *Adv. Mater.*, vol. 25, no. 24, pp. 3264–3294, Jun. 2013, doi: 10.1002/ADMA.201205076.

[30] S. Sharmin, A. Bosu, and S. Akter, "A Simple Gold-Coated Photonic Crystal Fiber Based Plasmonic Biosensor," *2018 Int. Conf. Adv. Electr. Electron. Eng. ICAEEE 2018*, Feb. 2019, doi: 10.1109/ICAEEE.2018.8643003.

[31] H. Abdullah, K. Ahmed, and S. A. Mitu, "Ultrahigh sensitivity refractive index biosensor based on gold coated nano-film photonic crystal fiber," *Results Phys.*, vol. 17, p. 103151, Jun. 2020, doi: 10.1016/j.rinp.2020.103151.

[32] A. Dinovitser *et al.*, "Exposed-core localized surface plasmon resonance biosensor," vol. 36, no. 8, Aug. 2019.

[33] A. Y. Pawar, D. D. Sonawane, K. B. Erande, and D. V. Derle, "Terahertz technology and its applications," *Drug Invention Today*, vol. 5, no. 2. pp. 157–163, Jun. 2013, doi: 10.1016/j.dit.2013.03.009.

[34] M. S. Islam, J. Sultana, A. Dinovitser, B. W. H. Ng, and D. Abbott, "A novel Zeonex based oligoporous-core photonic crystal fiber for polarization preserving terahertz applications," *Opt. Commun.*, 2018, doi: 10.1016/j.optcom.2017.12.061.

[35] M. Ahasan Habib, M. Shamim Anower, and M. Rabiul Hasan, "Highly birefringent and low effective material loss microstructure fiber for THz wave guidance," *Opt. Commun.*, 2018, doi: 10.1016/j.optcom.2018.04.022.

[36] A. Habib, "Ultra low loss and dispersion flattened microstructure fiber for terahertz applications," *Brill. Eng.*, 2020, doi: 10.36937/ben.2020.003.001.

[37] M. J. B. M. Leon and M. A. Kabir, "Design of a liquid sensing photonic crystal fiber with high sensitivity, bireferingence & low confinement loss," *Sens. Bio-Sensing Res.*, 2020, doi: 10.1016/j.sbsr.2020.100335.

[38] M. S. Islam *et al.*, "A novel approach for spectroscopic chemical identification using photonic crystal fiber in the terahertz regime," *IEEE Sens. J.*, 2018, doi: 10.1109/JSEN.2017.2775642.

[39] A. A. Rifat, G. A. Mahdiraji, Y. M. Sua, R. Ahmed, Y. G. Shee, and F. R. M. Adikan, "Highly sensitive multi-core flat fiber surface plasmon resonance refractive index sensor," *Opt. Express*, vol. 24, no. 3, p. 2485, Feb. 2016, doi: 10.1364/oe.24.002485.

[40] A. A. Rifat, G. Amouzad Mahdiraji, D. M. Chow, Y. G. Shee, R. Ahmed, and F. R. M. Adikan, "Photonic crystal fiber-based surface plasmon resonance sensor with selective analyte channels and graphene-silver deposited core," *Sensors (Switzerland)*, vol. 15, no. 5, pp. 11499–11510, 2015, doi: 10.3390/s150511499.

[41] M. N. Sakib *et al.*, "High performance dual core D-shape PCF-SPR sensor modeling employing gold coat," *Results Phys.*, vol. 15, p. 102788, Dec. 2019, doi: 10.1016/j.rinp.2019.102788.

[42] X. Yang, Y. Lu, B. Liu, and J. Yao, "Simultaneous measurement of refractive index and temperature based on SPR in D-shaped MOF," *Appl. Opt.*, vol. 56, no. 15, p. 4369, May 2017, doi: 10.1364/ao.56.004369.

[43] M. S. M. R. M. Islam *et al.*, "Design and Analysis of a Biochemical Sensor Based on Surface Plasmon Resonance with Ultra-high Sensitivity," *Plasmonics*, pp. 1–13, Jan. 2021, doi: 10.1007/s11468-020-01355-9.

[44] Y. Peng, J. Hou, Z. Huang, and Q. Lu, "Temperature sensor based on surface plasmon resonance within selectively coated photonic crystal fiber," *Appl. Opt.*, vol. 51, no. 26, pp. 6361–6367, Sep. 2012, doi: 10.1364/AO.51.006361.

[45] N. Cennamo, F. Arcadio, A. Minardo, D. Montemurro, and L. Zeni, "Experimental characterization of plasmonic sensors based on lab-built tapered plastic optical fibers," *Appl. Sci.*, vol. 10, no. 12, pp. 1–13, 2020, doi: 10.3390/app10124389.

[46] S. Chu *et al.*, "Influence of the Sub-Peak of Secondary Surface Plasmon Resonance onto the Sensing Performance of a D-Shaped Photonic Crystal Fibre Sensor," *IEEE Sens. J.*, vol.

21, no. 1, pp. 33–42, Jan. 2021, doi: 10.1109/JSEN.2019.2953393.

[47]   P. Bing *et al.*, "Analysis of Dual-Channel Simultaneous Detection of Photonic Crystal Fiber Sensors," *Plasmonics*, vol. 15, no. 4, pp. 1071–1076, Aug. 2020, doi: 10.1007/S11468-020-01131-9.

[48]   D. Pysz *et al.*, "Stack and draw fabrication of soft glass microstructured fiber optics," *Bull. Polish Acad. Sci. Tech. Sci.*, vol. 62, no. 4, pp. 667–682, 2014, doi: 10.2478/bpasts-2014-0073.

[49]   P. J. A. Sazio *et al.*, "Microstructured optical fibers as high-pressure microfluidic reactors," *Science (80-.).*, vol. 311, no. 5767, pp. 1583–1586, 2006, doi: 10.1126/science.1124281.

[50]   M. S. Islam *et al.*, "Dual-polarized highly sensitive plasmonic sensor in the visible to near-IR spectrum," *Opt. Express*, vol. 26, no. 23, p. 30347, 2018, doi: 10.1364/oe.26.030347.

[51]   J. N. Dash, R. Das, and R. Jha, "AZO coated microchannel incorporated PCF-based SPR sensor: A numerical analysis," *IEEE Photonics Technol. Lett.*, vol. 30, no. 11, pp. 1032–1035, Jun. 2018, doi: 10.1109/LPT.2018.2829920.

[52]   X. Meng *et al.*, "An optical-fiber sensor with double loss peaks based on surface plasmon resonance," *Optik (Stuttg).*, vol. 216, Aug. 2020, doi: 10.1016/J.IJLEO.2020.164938.

[53]   M. S. Aruna Gandhi, K. Senthilnathan, P. R. Babu, and Q. Li, "Highly sensitive localized surface plasmon polariton based d-type twin-hole photonic crystal fiber microbiosensor: Enhanced scheme for sers reinforcement," *Sensors (Switzerland)*, vol. 20, no. 18, pp. 1–13, Sep. 2020, doi: 10.3390/S20185248.

[54]   Y. Gamal, B. M. Younis, S. F. Hegazy, Y. Badr, M. F. O. Hameed, and S. S. A. Obayya, "Highly efficient modified dual D-shaped PCF polarization filter," *Opt. Fiber Technol.*, vol. 62, Mar. 2021, doi: 10.1016/J.YOFTE.2021.102459.

[55]   B. H. Almewafy, N. F. F. Areed, M. F. O. Hameed, and S. S. A. Obayya, "Modified D-shaped SPR PCF polarization filter at telecommunication wavelengths," *Opt. Quantum Electron.*, vol. 51, no. 6, Jun. 2019, doi: 10.1007/S11082-019-1885-X.

[56]   Z. Fan *et al.*, "Numerical Analysis of Polarization Filter Characteristics of D-Shaped Photonic Crystal Fiber Based on Surface Plasmon Resonance," *Plasmonics*, vol. 10, no. 3, pp. 675–680, Jun. 2015, doi: 10.1007/S11468-014-9853-6.

[57]   L. Yang *et al.*, "Design of bimetal-coated photonic crystal fiber filter based on surface plasmon resonance," *Results Opt.*, vol. 1, Nov. 2020, doi: 10.1016/J.RIO.2020.100027.

[58]   M. Li, L. Peng, G. Zhou, B. Li, Z. Hou, and C. Xia, "Design of Photonic Crystal Fiber Filter with Narrow Width and Single-Polarization Based on Surface Plasmon Resonance," *IEEE Photonics J.*, vol. 9, no. 3, Jun. 2017, doi: 10.1109/JPHOT.2017.2703979.

[59] J. Li, S. Li, S. Zhang, Y. Guo, and Y. Liu, "Broadband single-polarization filter of D-shaped photonic crystal fiber with a micro-opening based on surface plasmon resonance," *Appl. Opt. Vol. 57, Issue 27, pp. 8016-8022*, vol. 57, no. 27, pp. 8016–8022, Sep. 2018, doi: 10.1364/AO.57.008016.

List of publications

3) M. R. Islam , A. N. M. Iftekher, M. S. Anzum, M. Rahman and Sadia Siraz, "LSPR based Double Peak Double Plasmonic Layered Bent Core PCF-SPR sensor for Ultra-Broadband Dual Peak sensing", IEEE Sensors Journal, IEEE (February, 2022) **(Explained in chapter 8)**

http://dx.doi.org/10.1109/JSEN.2022.3149715

2) M. R. Islam, M. M. I. Khan, Sadia Siraz, F. Mehjabin, M. Rahman, M. Islam, M. S. Anzum, J. A. Chowdhury and F. Noor "Design and analysis of QC-SPR-PCF sensor for multipurpose sensing with supremely high FOM," Applied Nanoscience, Springer (November, 2021). **(Explained in chapter 7)**

https://doi.org/10.1007/s13204-021-02150-6

1) M. A. Islam, M. R. Islam, Sadia Siraz, M. Rahman, M. S. Anzum, and F. Noor, "Wheel structured Zeonex-based photonic crystal fiber sensor in THz regime for sensing milk," Applied Physics A, Springer (May, 2021) **(Explained in chapter 6)**

https://link.springer.com/article/10.1007/s00339-021-04472-2